

JPL Document D-1547413

TECHNOLOGY DEVELOPMENT FOR EXOPLANET MISSIONS

Technology Milestone #2 Final Report: Achromatic Visible Nulling Coronagraph Technology Maturation

Brian Hicks - University of Maryland College Park (UMCP)
Matthew Bolcar - Goddard Space Flight Center (GSFC)

Richard Lyon (PI), Mark Clampin (Co-I), Timothy Madison, Udayan Mallik, Patrick Thompson (GSFC), Peter Petrone III (Sigma Space Corp.) Michael Helmbrecht (Iris AO, Inc.)

July 11, 2016

National Aeronautics and Space Administration

Jet Propulsion Laboratory
California Institute of Technology
Pasadena, California

Approvals

Released by

Brian Hicks
Science Principal Investigator

Matthew Bolcar
Acting Principal Investigator

Mark Clampin
Co-Investigator

Approved by

Nick Siegler
Exoplanet Exploration Program Chief Technologist, JPL

Gary Blackwood
Exoplanet Exploration Program Manager, JPL

Douglas Hudgins
Exoplanet Exploration Program Scientist, NASA HQ

Contents

- Executive Summary 4
- 1 Introduction 4
- 2 Theoretical approach to the VNC broadband effort 5
- 3 The Milestone Procedure 7
 - 3.1 Top-Level Description 7
 - 3.2 Detailed Description of Broadband Wavefront Sensing and Control Efforts 7
 - 3.3 Focal Plane Contrast Measurement Steps in a Data Collection Event 11
 - 3.4 Milestone Validation Procedure 15
- 4 Success Criteria 15
 - 4.1 Spectral Bandpass 15
 - 4.2 Contrast 15
 - 4.3 Confidence 15
 - 4.4 Repeatability 16
- 5 Demonstration Narrative 16
 - 5.1 Design, procurement, and installation of achromatic phase shifters (APS) 16
 - 5.2 Dark channel detector upgrade 18
 - 5.3 Control rate adjustments 21
 - 5.4 Full-yield segmented DM testing 22
 - 5.5 Filter bandpass measurements and source characteristics 22
 - 5.6 Vacuum leak rates and outgassing tests 23
 - 5.7 Stability measurements 23
- 6 Results and lessons learned 25
 - 6.1 Known issues to be addressed in future efforts 25
- 7 Milestone Certification Data Package 31
- 8 Summary and Future Milestones 32

Acronyms

ADU - Analog to Digital Units
AOI - Angle of Incidence
APS - Achromatic Phase Shifter
ARMA - Auto-Regressive Moving Average
COTS - Commercial, Off-the-Shelf
CPA - Cycles Per Aperture
CVNT - Compact Visible Nulling Testbed
DCE - Data Collection Event
DM - Deformable Mirror
ETU - Engineering Test Unit
FBA - Fiber Bundle Array
GSFC - Goddard Space Flight Center
HabEx - The Habitable Exoplanet Imager
IRAD - Internal Research and Development
IWA - Inner Working Angle
LUVOIR - Large UV/Optical/InfraRed
MEMS - Microelectromechanical Systems
MMA - Multiple Mirror Array, a.k.a. (hex-packed) segmented MEMS DM
MPI - Message Passing Interface
OPD - Optical Path Difference
PSF - Point Spread Function
PTT - Piston-Tip-Tilt (or piston, tip, and tilt)
PZT - Piezoelectric Transducer (or “piezo”)
RMS - Root Mean Square
ROI - Region of Interest
RTOS - Real Time Operating System
SAT - Strategic Astrophysics Technology
SBIR - Small Business Innovation Research
SAINT - Segmented Interferometric Interferometric Nulling Testbed
SDK - Software Development Kit
SFA - Spatial Filter Array
TAC - Technical Advisory Committee
TIR - Total Internal Reflection
TDEM - Technology Development for Exoplanet Missions
TRL - Technology Readiness Level
VNC - Visible Nulling Coronagraph
VNT - Vacuum Nuller Testbed
WFC - Wavefront Control
WFE - Wavefront Error
WFS - Wavefront Sensing

Executive Summary

The direct detection and spectroscopic characterization of exoplanets in our local neighborhood requires starlight to be suppressed relative to the planet at small angular separations. The Visible Nulling Coronagraph (VNC) is a strong candidate for an internal coronagraph capable of achieving high-contrast imaging with either filled, segmented, or sparse/dilute aperture telescopes. Past and ongoing work are leveraged with lessons learned from the Vacuum Nuller Testbed (VNT) to build an achromatic Compact Visible Nulling Testbed (CVNT) to serve as an Engineering Test Unit (ETU) and advance the VNC from its current NASA Technology Readiness Level (TRL) of 4 to TRL 5. The VNT achieved $> 10^8$ contrast at an inner working angle (IWA) of $2\lambda/D$ through the use of a multiple mirror array (MMA) – a hex-packed microelectromechanical (MEMS)-based deformable mirror (DM). The system uses interferometric wavefront sensing (WFS) to perform wavefront control (WFC) using all available starlight.

The TDEM-10 “Compact Achromatic Visible Nulling Coronagraph Technology Maturation” proposed by PI R. Lyon and the VNC team set forth to complete the development of an ETU and achieve $> 10^9$ contrast at $2\lambda/D$ over a 40 nm bandpass centered at 633 nm. Unlike the breadboard VNC, the CVNT is intended to be operated in a vacuum environment and advance the concept to NASA TRL 5.

The Milestone goals were not met in this effort. It had been intended that PI R. Lyon would be running the control system as he did for TDEM Milestone #1 (PI Clampin), with B. Hicks focused on the optics and hardware portion of the the Milestone #2 task: upgrading components of the VNC including designing, procuring, installing, aligning the APSs, integrating a new detector, and making the requisite vacuum system modifications and preparations. In light of the unknown nature of when he would be back to full health, R. Lyon transferred as much knowledge of the VNC control code as possible to B. Hicks, predominantly via phone and email while being encumbered by poor health throughout 2014 and 2015 with a period of being completely unavailable in the end of 2014 through early 2015. Ultimately, R. Lyon’s untimely death in early 2016 has culminated in the team running out of time to address all known issues that are suspected of having impeded reaching the Milestone goal that hinges on closing the loop on fast wavefront control.

This report provides a narrative of what was accomplished, including lessons learned, and a prospectus for streamlining and improving the development of the VNC toward a higher-fidelity ETU (summarized in Tab. 5 near the end of this document). The lessons learned from this effort should provide guidance on viable options for future space-based missions such as the Habitable Exoplanet Imager (HabEx) or a large UV-Optical-Infrared (LUVOIR) surveyor[1], formerly studied as the Advanced Technology Large Aperture Space Telescope (ATLAST), which is currently favored to be a 10-m or greater segmented aperture[2, 3, 4]

1 Introduction

Direct detection and characterization of exoplanetary systems around stars including exoplanets, dust, and debris disks, are all goals for understanding the evolution of and search for planets in spectral type-dependent habitable zone orbits. Through the measurement of atmospheric spectral signatures, Earth-sized planets with molecular abundances similar to what we associate as being necessary for sustaining life as we know it may be identified. The VNC is an approach to high-contrast imaging being developed to enable such observations at both the component- and system-level. This approach has been proposed for both probe-class[5] and stratospheric balloon[6] missions. The VNC is an interferometer that suppresses starlight in one of its outputs to enable high-contrast detection, while shifting the starlight to the other output for instrument control. As a breadboard instrument, the VNC has demonstrated $> 10^8$ contrast averaged over an inner to outer working angle of $1 - 4\lambda/D$ in polarized narrowband (1.2 nm FWHM) light.[7, 8] This is the level and separation required to detect and characterize dust, debris disks, and exo-Jupiters in nearby systems. At the system-level, the VNC is a viable option for a variety of planned mission telescope architectures, including the obscured 2.4-m Wide-Field Infrared Survey Telescope (WFIRST) aperture.[9] In the more distant future, the VNC could be a high-contrast imaging instrument for HabEx or a LUVOIR surveyor.

Application of the VNC spans all future flight telescope architectures including monolithic (both off-axis

unobscured and on-axis obscured), segmented, dilute, and sparse aperture telescope systems. Additionally, the VNC makes use of all the available output photons for null control since the flux from the target star is conserved in the bright and dark output channels. This conservation law yields a robust null control approach that is independent of the state of the instrument with a control temporal bandwidth that depends only on the brightness of the target star. In theory, it does not levy beyond state of the art telescope stability requirements since the telescope must be stable only over each integration window for null control.

This work describes progress toward achieving 10^{-9} contrast with the VNC at an increased spectral bandpass of 40 nm FWHM using polarized, and later unpolarized, sources. We present a summary of the design and status report on the VNC broadband demonstration following the addition of Fresnel rhombs as Achromatic Phase Shifters (APS) and a dark channel detector upgrade.

2 Theoretical approach to the VNC broadband effort

Scattered starlight suppression at the level of $< 10^{-9}$ contrast has yet to be demonstrated broadband (5 – 20%) with a system that maintains high throughput ($> 10\%$) and off-axis transmission at small separation angles ($< 3\lambda/D$) with a non-circular pupil. In principle, the VNC can achieve all of these performance metrics. The key ability of broadband operation increases sensitivity for discovery and enables spectroscopic characterization of exoplanets. For a nulling interferometer (nuller), such as the VNC, operating broadband requires introducing a quasi-achromatic destructive interference condition over as large a coronagraphic region as possible in the science focal plane. Our effort hinges on applying the phenomenon of optical retardance to accomplish broadband destructive interference. The retardance effect is manifested as a difference in phase shift between orthogonal polarization components introduced by an optical element or interface. Crossed Fresnel rhomb pairs provide a means by which a retardance-based π phase delay can be introduced between interferometer arms[10], and studies suggested that this approach could be used to reach the VNC broadband milestone targeting a 6% visible bandpass.[11] Fig. 1 symbolically presents the principle of this polarization-based nulling.

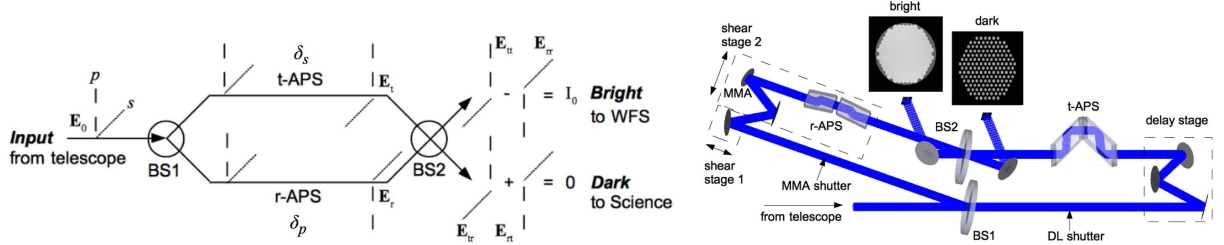


Figure 1: *Left:* The principle of polarization-based interferometric nulling. The dashed and dotted lines representing the respective p- and s-polarization components relative to the beamsplitter (BS1) and beamsplitter/combiner (BS2) are imparted with orthogonal $\delta = \pi$ retardance in each arm. The subscripts t and r denote beamsplitter reflection and transmission, respectively. Beamsplitter and common phase factors introduced by fold mirrors, path, and the Fresnel rhombs are not indicated in the orientation of the polarization components to emphasize the effect of the rhombs. *Right:* The VNC model for performing sensitivity and compensation analysis used to tolerance the Fresnel rhombs APS that have been fabricated and integrated with the VNC to demonstrate 10^{-9} contrast over a 40 nm bandwidth centered at 633 nm. The APS consists of two pairs of symmetric Fresnel rhombs. The pairs are oriented orthogonally to one another relative to their respective nominal total internal reflection (TIR) polarization s- and p-planes.

Following a recent work treating the retarders as an arbitrary pair of elements[12], one in each arm of an interferometer, the system is fed with an input field of some polarization state, which for simplicity here is assumed to be linear,

$$\mathbf{E}_0 = E_0 \begin{pmatrix} \cos \theta \\ \sin \theta \end{pmatrix}, \quad (1)$$

where θ is the polarization angle measured about the axis of propagation relative to some reference surface,

e.g., the first beamsplitter. Real beamsplitters and retarders influence the complex wavefront in a chromatic and polarization dependent manner. Omitting common phase factors due to path and fold mirrors, following traversal of the first beamsplitter and retarders, the fields in each arm may be written as

$$\mathbf{E}_t = E_0 \begin{pmatrix} t_s e^{i\delta} \cos \theta \\ t_p \sin \theta \end{pmatrix} \quad (2)$$

$$\mathbf{E}_r = E_0 \begin{pmatrix} r_s e^{i\xi_s} \cos \theta \\ r_p e^{i(\delta+\xi_p)} \sin \theta \end{pmatrix} \quad (3)$$

where the subscripts s and p correspond to polarization components relative to the beamsplitter, r and t denote reflected or reflectance and transmitted or transmittance, respectively, and ξ is the difference in phase between the reflected and transmitted beams, and the fields are imparted with phase retardance at orthogonal orientations relative to the input field. For TIR the phase shifts imparted to the s - and p -components of the electric field are

$$\phi_s = -2 \tan^{-1} \left[\frac{\sqrt{\sin^2 \gamma - n^2}}{\cos \gamma} \right] + \pi \quad (4)$$

$$\phi_p = -2 \tan^{-1} \left[\frac{\sqrt{\sin^2 \gamma - n^2}}{n^2 \cos \gamma} \right] \quad (5)$$

where $n(\lambda) = n_a/n_g$ is the ratio of the ambient index of refraction, n_a , to that of the glass, n_g , and retardance is defined as

$$\delta = \phi_p - \phi_s + \pi. \quad (6)$$

By choosing an appropriate prism material of index $n_g(\lambda)$ and angle of incidence (AOI) γ , the $\delta - \pi/4$ retardance for a single TIR can be minimized such that after four reflections the total retardance is identically π at some wavelength within the design bandpass (see Sec. 5.1 and Fig. 9). Since the phase retardance is imparted through TIR, there is no diattenuation.

Following recombination, the bright, asymmetric output fields may be written as

$$\mathbf{E}_{tt} = E_0 \begin{pmatrix} t_s^2 e^{i\delta} \cos \theta \\ t_p^2 \sin \theta \end{pmatrix} \quad (7)$$

$$\mathbf{E}_{rr} = E_0 \begin{pmatrix} r_s^2 e^{i2\xi_s} \cos \theta \\ r_p^2 e^{i(\delta+2\xi_p)} \sin \theta \end{pmatrix} \quad (8)$$

and the fields in the dark, symmetric output are

$$\mathbf{E}_{tr} = E_0 \begin{pmatrix} t_s r_s e^{i(\delta+\xi_s)} \cos \theta \\ t_p r_p e^{i\xi_p} \sin \theta \end{pmatrix} \quad (9)$$

$$\mathbf{E}_{rt} = E_0 \begin{pmatrix} r_s t_s e^{i\xi_s} \cos \theta \\ r_p t_p e^{i(\delta+\xi_p)} \sin \theta \end{pmatrix} \quad (10)$$

For the ideal $\delta = \pi$ retarder used with a lossless, polarization-independent 50/50 beamsplitter ($\xi = \pi/2$), the bright and dark output intensities are

$$I_b = |\mathbf{E}_{tt} + \mathbf{E}_{rr}|^2 = \frac{I_0}{2} (1 - \cos \delta) \quad (11)$$

$$I_d = |\mathbf{E}_{tr} + \mathbf{E}_{rt}|^2 = \frac{I_0}{2} (1 + \cos \delta) \quad (12)$$

which evaluates to $I_b = I_0$ and $I_d = 0$ when retardance in each arm, $\delta = \pi$. Total leakage attributed to errors in the broadband retardance across a design bandpass may be approximated by Taylor series expansion of Eq. 12 about $\delta = \pi$

$$L_\delta = \sigma_\delta^2 / 4 \quad (13)$$

where σ_δ is the rms retardance error over the design bandpass. The equations above were used to design and tolerance a set of Fresnel rhombs that were fabricated and incorporated into the VNC to meet the Milestone goals for this demonstration. The theoretical performance of the rhombs is presented in Sec. 5.1.

3 The Milestone Procedure

3.1 Top-Level Description

Milestone #2 requires laboratory intensity measurement of light in the dark focal plane after suppression relative to the intensity in the dark focal plane without suppression. This measurement is made as a function of focal plane location. No beam shear is used in this demonstration, which effectively nulls all of object space.

At the top-level, the measurement process is a two-cycle process. The first step, known as the calibration cycle, refers to balancing and measuring the flux in both the MMA and delay line arms of the interferometer. The second step, known as the dark cycle, refers to driving the piston delay mechanisms, Fresnel rhomb APS, and MMA such that off-axis flux in a targeted region of interest is minimized, collecting a set of images while holding the averaged off-axis counts in this region at a minimum using wavefront sensing (WFS) and wavefront control (WFC), or WFS/C.

The VNC uses a hexagonally-packed segmented DM[13], also referred to as a multiple mirror array (MMA) to distinguish it from a continuous facesheet DM, which has actuators that are inherently coupled with their nearest neighbors. The MMA is used for phase control across the instrument beam to compensate for surface errors and coating and asymmetries introduced by elements in the optical train. The VNC approach to WFS/C is described in more detail in other recent works.[7, 11] Here it suffices to state that wavefront control is performed in such a way to balance phase, amplitude, and polarization effects to optimize contrast within a range of spatial frequencies corresponding to the dark hole region of the high-contrast (science) image focal plane.

3.2 Detailed Description of Broadband Wavefront Sensing and Control Efforts

There are two main control components of the VNC WFS/C: (1) low spatial frequency polychromatic π phase shifting achieved between interfering “arms” with zero optical optical path difference (OPD) and careful positioning of the orthogonal half-wave Fresnel rhomb pairs that comprise the APS, and (2) high spatial frequency correction using a deformable mirror, the MMA, located at a pupil in one arm of the muller cavity. The layout of these components is shown in Fig. 1. The APS introduces a new addition to the VNC.

The largest optimized dark region (“dark hole”) size that can be achieved with a continuous facesheet DM scales as a Nyquist limited controller. Assuming a 64×64 Cartesian grid, the Nyquist limit would give 32 cycles per aperture (CPA). A typical point spread function (PSF) has a $\sim \rho^3$ tail attributed to a combination of diffraction through the aperture and surface scattering, where ρ is the off-axis angle. As such, when optimizing the dark hole from $2 - 32\lambda/D$, the flux outside of $32\lambda/D$ spills some flux back into the dark hole due to the sum of all the tails since each speckle is really a PSF. This becomes a limiting factor on contrast and it depends on the power spectral distribution of the wavefront error (WFE). A segmented DM, fits both local piston and local slope. Breaking the surface into Zernike terms fitted at each point along surface tangents gives a smaller RMS fitting error.[14] In the 1D case, given a segmented DM with 64 segments in linear extent, corrections can also be made out to 32 CPA. Adding the second dimension, three points defining a plane are fit to a 2D surface. The hexagonal geometry complicates analytical calculations of fitting errors and in general the wavefront control problem is addressed numerically.

For higher-order spatial frequency WFC, the VNC uses the MMA to first suppress the pupil, then optimize contrast within the targeted region of high contrast. Controlling each of the MMA’s hexagonal segments in piston, tip, and tilt (PTT) by three voltage-driven actuators in closed-loop allows the VNC to increase the contrast within the dark hole. Iterative closed-loop control allows deeper contrast to be obtained and held. Each actuator voltage is controlled in software. Each of the MMA segments’ PTT influence functions are orthogonal, i.e., motion of any one segment in either piston, tip, or tilt does not influence its other other two degrees of freedom or its neighbors. However, since we desire a dark hole in a specific focal plane region, it is more efficient to couple linear combinations of actuators together into a set of control modes. This

results in a smaller set of control modes enabling a trade between higher control bandwidth and instrument-level temporal stability. The optimal control mode set depends on the size and location of the dark hole region and on the sensing noise floor due to vibration and detector noise. A description of the routine for generating MMA null control modes (see Fig. 2) developed by R. Lyon for the VNC narrowband Milestone # 1 is presented in that effort’s report[8] and is not repeated in this Milestone Report.

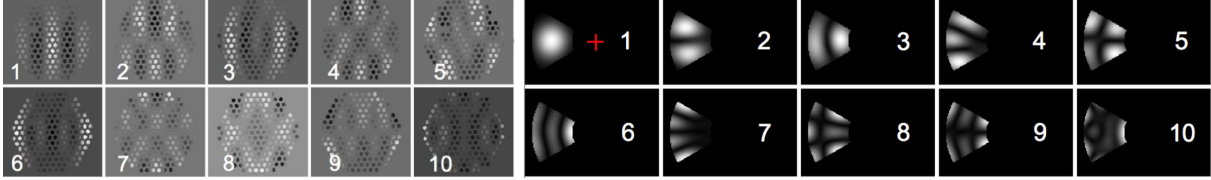


Figure 2: The first ten of 200 MMA control modes (*left*) and corresponding focal plane intensity patterns of greatest influence for optimizing the VNC dark hole (*right*). The red cross indicates the center of the on-axis PSF.

The contrast measurement requires a measurement of the focal plane intensity averaged over multiple frames comprising successive time windows of multiple frames. Statistical measures are used to assess confidence and to minimize the impact of noise and uncertainties. The following provide a series of definitions followed by a delineation of the step-by-step procedure for the measurement process (Sec. 3.3). A listing of demonstration Success Criteria and components of the Data Certification Package are provided respectively in Sec. 4 and toward the end of this Report in Sec. 7.

Raw and Calibrated Images

“Raw” images are the pixelated images directly output by both the bright and dark channel detectors. The bright images are in units of analog to digital units (ADU), i.e., detector counts, and the dark channel images are in units of photon counts. The 16-bit camera is operated at or near 80% full well to avoid saturation. “Calibrated” images are processed in situ to subtract dark frames and flat-fielding. The aggregate set of raw and calibrated images generated in this Milestone #2 effort are archived in a set of CDs available for further analysis as required.

Plate scale calculation

The dark detector plate scale is determined by fitting a simulated PSF corresponding to the hexagonal array of circular subapertures corresponding to the Lyot mask aperture function[8, 15] to calibrated images generated by alternately closing shutters in each arm of the interferometer. Preference is given to the reference arm if the MMA is not in a flattened state. Fig. 3 shows the simulated PSF, sample calibrated frame data for each arm, and the incoherent sum of both arms, along with the difference between the simulated and calibrated (incoherently summed) frames.

Each data frame is 512x512 pixels and the simulated PSF dimensions are 48x48 λ/D resulting in a calculated plate scale of 0.09375 λ/D per pixel, or 10.667 pixels per λ/D . The rotation of the image on the detector is attributed to folding in the VNC aft-optics, which includes a periscope with a diverging lens between the two persicope mirrors. The simulated PSF on the left in each image is identical, and is a simulated $\sim 5\%$ bandpass to match the 31.7 nm centered on 654.7 nm bandpass filter (see Sec. 5.5).

Contrast Images

For the lab VNC, contrast is defined by $C = F_{min}/(F_{MMA} + F_{delay}) = F_{min}/F_{inc}$ where F_{min} , F_{MMA} , and F_{delay} are the background subtracted frames corresponding respectively to conditions of destructive interference (i.e., “suppression”), and alternately blocking the delay, then MMA arm of the interferometer using shutters. The individual beams summed as $F_{inc} = F_{MMA} + F_{delay}$ define the incoherent or unsuppressed source intensity distribution. Suppression occurs after driving the piston mechanism and MMA to minimize

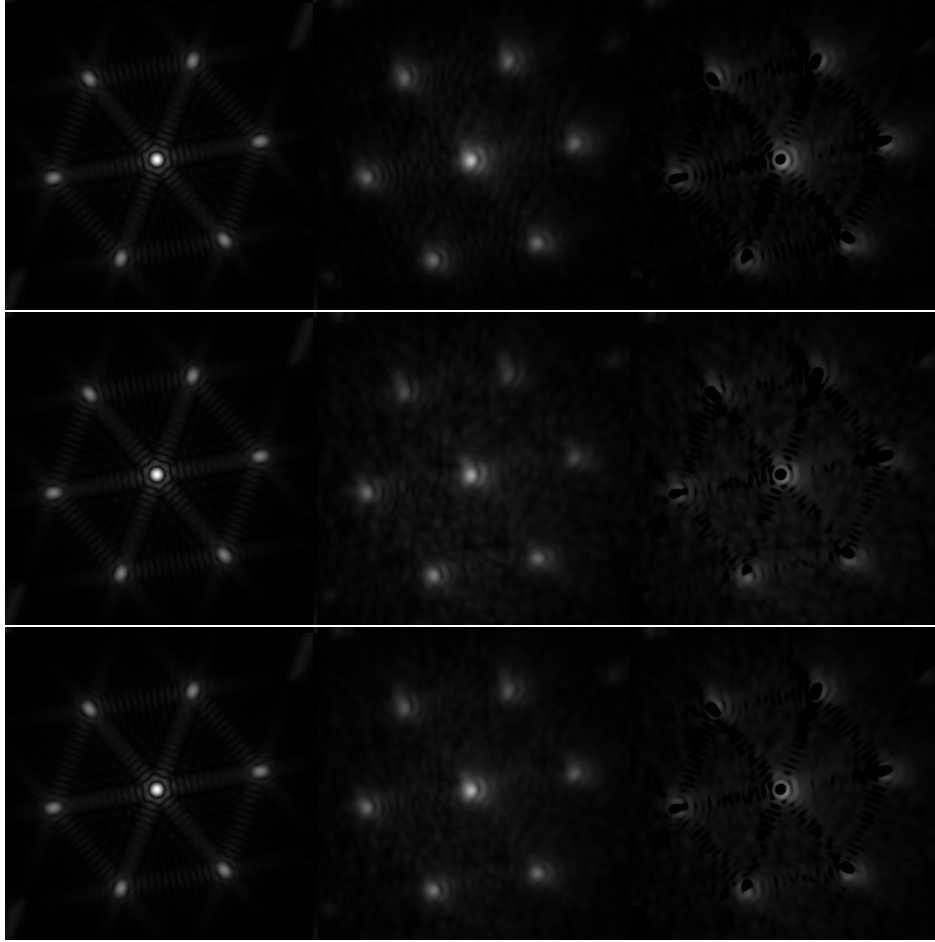


Figure 3: *From left to right:* simulated PSF, dark channel output, and the difference of the two used to calculate plate scale for from top to bottom, the delay arm, the MMA arm, and the sum of the two independent arms. The PSFs are stretched by $I^{1/4}$ to improve visibility of the six sidelobes centered on the PSF core azimuthally spaced at 60° . Each 512×512 frame is $48x48\lambda/D$ in extent.

the detector counts at the specified off-axis location in the focal plane. The ratio of the peak of the incoherent sum and suppressed images should reach $\sim 10^{-4}$ to 10^{-5} at the center of the focal plane, i.e., at $0\lambda/D$ before fine control is implemented to optimize the high-contrast region of interest. The off-axis location where control algorithm measurements are made is at an angular separation of $2\lambda/D$ extending over a circular mask of diameter $1\lambda/D$ (see Fig. 4). At this demonstrations plate scale of $10.667\lambda/D$, $2\lambda/D$ falls at 21.334 detector pixels from the center of the PSF and the diameter of the mask is 10.667 detector pixels. There are 1244 pixels within the full mask, and 89 pixels within the $1\lambda/D$ diameter circle centered at $2\lambda/D$.

Contrast is estimated from the photoelectron count in each detector pixel focal plane location, θ . The goal was to measure contrast for multiple realizations, each being referred to as a Data Collection Event (DCE). A “realization” consists of multiple closed-loop control steps with an auto-regressive moving average (ARMA) approach to feeding back the actuator voltages to minimize the effect of photon noise. A single realization consists of averaged contrast maps over many closed-loop control steps.

VNC Control Algorithms

The VNC control algorithms consist of a sequence of steps shown in Fig. 5 and described in greater detail in Sec. 3.3 below. Coarse phasing algorithms are intended to bring the VNC from up to millimeters down

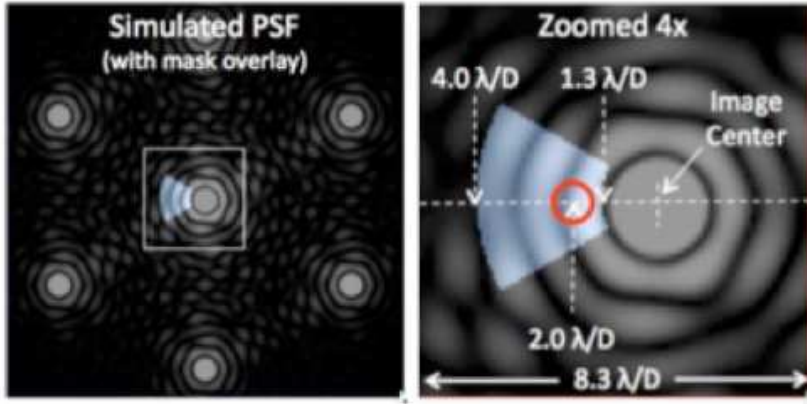


Figure 4: A simulated high-contrast focal plane and high-contrast region of interest. The left panel is $34.7\lambda/D$ in extent, showing the VNC focal plane on log-scale where blue shows the targeted region of highest contrast for which MMA control modes are generated. The right panel shows a zoom of the high contrast region over which the Milestone is to be assessed, the red circle of diameter $1\lambda/D$ centered at $2\lambda/D$.

to less than one wave of path error between arms. Fine-tuning algorithms further reduce phase error in the system to < 10 nm RMS WFE, and then holds the WFE at or below this value.

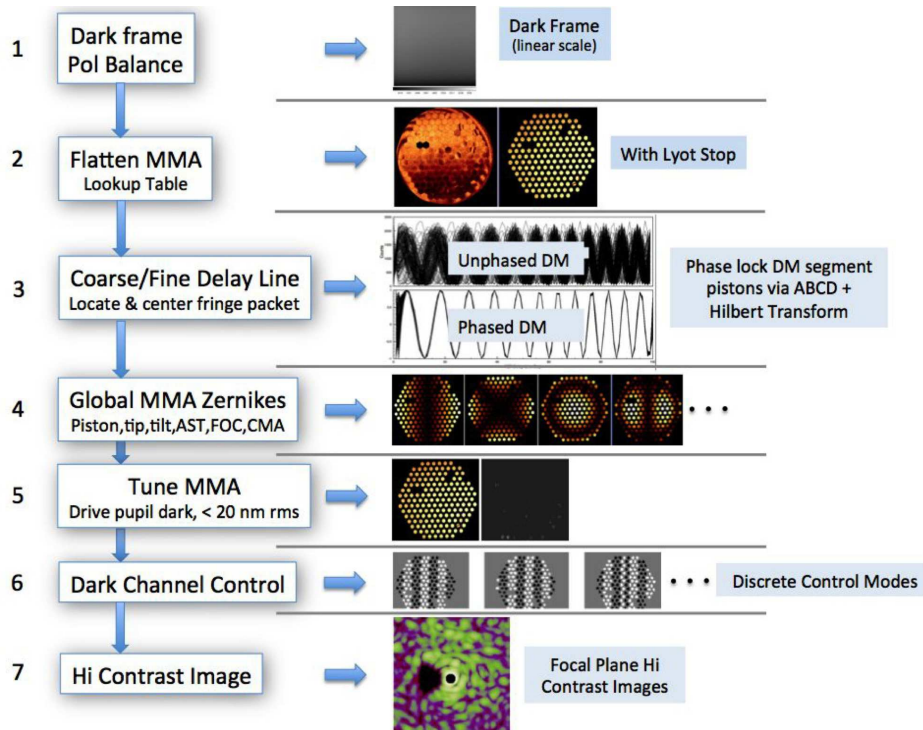


Figure 5: The VNC null control sequence (from the VNC narrowband TDEM #1 Milestone Final Report[8])

The algorithmic steps shown in Fig. 5 are designed to operate as a cascaded servo: each step transitions to the next as a weighted sum of the current algorithm and its predecessor. It should be noted that wavefront control is accomplished from the pupil and focal planes and no discrete optics are moved into or out of the system during operation. The only moving components during contrast measurements are the individual mirror segments of the MMA, and the piston mechanism which moves over a maximum range of ~ 160 nm during closed-loop operation.

Algorithm (2) consists of instantly applying a lookup table to the MMA. Algorithm (3) moves the delay and uses a variation of a phase-shifting interferometry algorithm. This typically takes several minutes to bring the rms WFE to ~ 20 nm. Algorithm (4) takes approximately 1 minute and is mostly concerned with tuning overall beam focus and segment level piston/tip/tilt to better place the focal plane image. Algorithm

(3) and (4) are iterated several times, involving motion of both the MMA segments and the delay line such that the average delay offset is approximately the average over the set of MMA pistons ensuring that the segments are at or near the center of their range to maximize control dynamic range. Algorithm (5) takes several minutes and is used to drive the pupil dark and to collect the bright frames in the focused image for contrast calculation. At the end of algorithm (5), the MMA is moved in pure piston to invert the dark pupil to a bright pupil and thereby darken the focal channel image. From an energy conservation standpoint, tuning of the MMA makes the bright pupil image as bright as possible. At this point, the hand-off to the fine control is initiated by running the dark channel modal control that moves a linear combination of actuators to build the dark hole and progressively lower mean counts over the region of the mask, holding it as dark as possible. This is more time-consuming and takes tens of minutes to lower the dark hole to $\sim 10^{-8}$. Large disturbances that result in an out-of-spec condition are gradually dampened out. Simulated cases exhibiting this behavior are presented in Fig. 6.

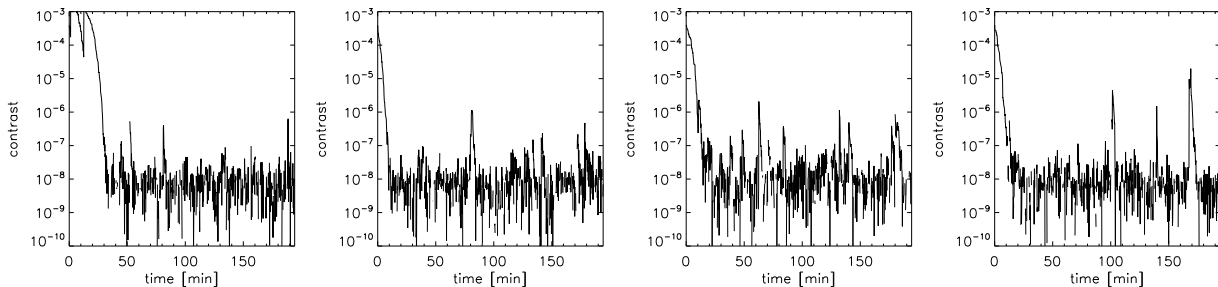


Figure 6: Simulations of 10^{-8} convergence timescales associated with 1 \AA RMS jitter, 2.5 ADU read noise, and a starting error of 40 nm. The single frame count maximum at the associated contrast is 80% of full well and a θ^{-3} roll-off at $2\lambda/D$ is applied. 70 control modes are assumed[7] running at a control bandwidth of 6 Hz. Both environmental disturbances and sensing errors due to read noise are modeled causing contrast to periodically exceed 10^{-8} .

Data Collection Event

A data collection event (DCE) takes place over the course of hours and in its final stage consists of a shorter sequence of thousands of 512×512 images acquired over a period of 1000 seconds as prescribed by the Success Criteria in Sec. 4. The 1000 second interval is the aggregate time when algorithm (6) described in Sec. 3.3 is used for contrast and does not include the times for algorithms (1) through (5). A full DCE lasts longer than 1000 seconds, but it is only the data collected during this last period that is used to calculate contrast for the Milestone. The time prior to this is spent performing coarser phasing and building the dark hole. Using calibrated data obtained during fine control corresponding to algorithm (6) performed at a rate of ~ 6 Hz, contrasts are calculated according to algorithm (7) as described above and shown in Fig. 5.

3.3 Focal Plane Contrast Measurement Steps in a Data Collection Event

The focal plane contrast measurement steps are described in this section, and this section has been revised from the whitepaper. This was deemed necessary as the sensing and control of the VNC and MMA has significantly advanced since this effort was proposed. All output images are saved during the Calibration sequence and during Algorithms (1) and (2) as FITS files, however during fast closed-loop control, all images are not saved as the time to collect, format, and write images to a disk, largely due to time required to transfer and analyze such a large number of files. Final contrast images are saved at a rate of ~ 1 per 0.167 seconds.

Null Control

Initialization consists of first turning on the source, the cameras and camera chillers, then waiting for the system to stabilize. It is noted that vacuum pumping would occur at this point and then be switched off for final tests at < 0.01 atm following closed-chamber operation at 1atm. While this capability has been established (see Sec. 5.6), due to not having achieved closed-loop control, the planned final low-pressure demonstrations of VNC operation were not performed. Next, amplifiers for driving the MMA, piston/shear mechanisms, and the APS fine-positioning are switched on, and the data processing interface to these systems are booted. The MMA is then commanded to a preset “flat” setting that has been pre-determined to off-load substrate bowing, nominally setting all MMA segments to provide a composite WFE < 60 nm RMS. The coarse and fine piston mechanisms are actuated such that the fine piston mechanism is set near midrange at zero OPD between arms.

The null control sequence consists of the series of seven high-level steps shown in Fig. 5. The null control sequence uses images from the bright pupil camera and dark focal plane camera to both reduce the mean and the RMS (WFE) and subsequently control a specific range of modes (spatial frequencies) to obtain and hold a dark-hole at a specific location in the focal plane. The mean WFE is the piston difference between the two arms of the interferometer and it controls the overall irradiance of the dark focal plane image. The ideal mean wavefront error is at zero path delay since phase shifting is achieved by the Fresnel rhomb retardance. In practice zero path delay is located using open-loop PZT scanning of the fringe packet in discrete steps targeting nulling of the core to $< 10^{-3}$. The remaining control sequence steps lower the RMS wavefront error over a range of spatial frequencies sufficient to optimize a dark-hole $\leq 10^{-8}$ for working angles ranging from 1.5 to $4\lambda/D$.

Each step in the process is designed to introduce less spatial correlation in the wavefront error across the pupil. Moving the delay only imposes a global wavefront change across the entire pupil, while moving global Zernike modes imposes wavefront changes that vary across the pupil but with long correlation lengths, i.e., low spatial frequencies. Application of the discrete modes controls a narrow range of spatial frequencies. Individual MMA segments have the shortest correlation length and control the highest spatial frequencies. This approach effectively bootstraps from lower to higher spatial frequencies.

1: Polarization Balance & Dark Frame Acquisition

Polarization balance corrects the mean intensity difference between the two arms of the interferometer to $< 1\%$. This is accomplished by a linear polarizer before the first beamsplitter, one linear polarizer in each of the two interferometer arms, and a linear polarizer after the beam combining beamsplitter at each of the cameras, i.e., four linear polarizers in all. All the polarizers are set to the same axis before insertion into the interferometer. A sequence of images are collected with both interferometer arm shutters closed followed by a sequence with one shutter open and another sequence with the other shutter open, i.e., only one shutter within the interferometer is open at a given time. Each of the image sequences is averaged and the detector counts totaled and the mean difference tabulated. This is repeated after rotating the polarizer in the interferometer arm with the greatest intensity to match the arm with the lower intensity. This is repeated until balanced as best as possible. Acquiring dark frames is a standard calibration approach for the detectors and consists of collecting frames with the source off (bias frame), source on but shutters closed (dark frame), and ramping the integration time to obtain the gain (photo-electrons/ADU) for each camera pixel. This calibration is performed at the outset of the data collection events.

2: Flatten the Multiple Mirror Array

Flattening the MMA employs using a lookup table to command each of the segments in piston, tip and tilt to nominally minimize the WFE between the two interferometer arms. The lookup table is periodically generated by using a 5-bucket interferometer algorithm (see e.g., [16] and references therein). At this step the WFE should typically reach 20–40 nm RMS. The spread is caused by slow thermal drift in the optics mounts. Newly generated lookup tables nominally reach ~ 20 nm RMS, whereas after three or four days

in a stable environment the system drifts and can exceed ~ 40 nm RMS. The VNC control software toolkit includes an automated means of scanning both the MMA and piezoelectric transducer (PZT or “piezo”) actuator to minimize the piston across the array and match the phase profile of the reference (delay) arm of the interferometer. An additional tool was developed to perform iterative updates to the flats file piston terms using a Gaussian fit to the absolute value of each segment’s mean-subtracted fringe packet.

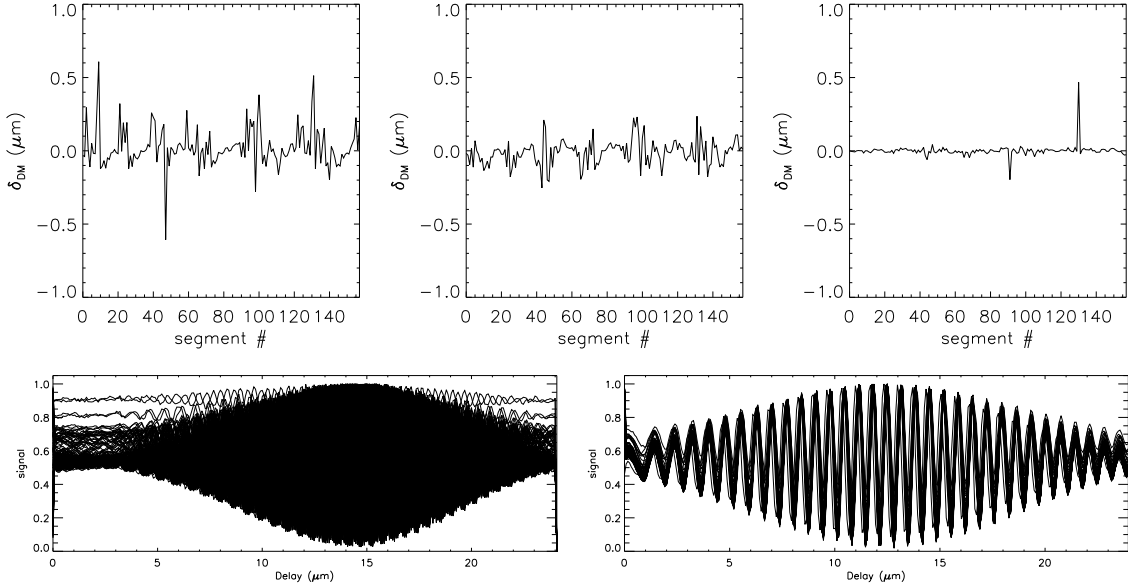


Figure 7: The top plots show a progressive reduction in phase error for each MMA segment relative to their mean piston value using an iterative approach of fine scanning the PZT through the full broadband fringe packet. The bottom plots show an overlay of the fringe packets for each segment before (*left*) and after (*right*) applying calculated offsets to the lookup flats file piston values. The low visibility scans in the unphased plot are attributed to segment tilt, which has been corrected using various automated methods and editing the flats file “by hand.”

3. Coarse and Fine Delay Line

Setting the coarse and fine delay line refers to moving the mechanical delay followed by fine-tuning with a piezo-mounted on the head of the stepper actuator. The mechanical delay uses a straightforward approach that steps the delay line continuously such that the bright pupil image is sampled at intervals of 150 nm. Significant modulation of the pupil image is observed when the path difference between the interferometer is less than the coherence length of $\lambda^2/\Delta\lambda \sim 0.3$ mm. The variance of the counts of images within the coherence length is higher than when outside the coherence length, and this is exploited to set the coarse mechanical delay such that the OPD is within the interferometric fringe “packet.” Once at this position, the fine delay line is stepped in ~ 20 nm increments over the entire fringe packet to set the fine delay. When operating in narrowband light, the required scan range for finding the central fringe is hundreds of micrometers due to the long coherence length, i.e., high fringe visibility over many waves. For broadband operation using the widest bandpass filter available for this demonstration, the scan range is only approximately 5 μm (see Fig. 7 and Tab. 4).

4. Global MMA Zernikes

Setting global MMA Zernikes refers to using low-order spatially-correlated Zernike polynomial modes imposed by moving the MMA segments in PTT as a low-order ensemble to match the MMA arm PSF core to that of the delay arm. Global piston, tip, tilt, astigmatism, focus, coma, trefoil and spherical aberration Zernike modes are also used.

5: Tune MMA

Tuning the MMA refers to moving individual segments of the MMA in local piston, tip and tilt, to minimize the counts in the pupil image, i.e., to drive it as dark as possible to the noise floor of the camera. These motions move only a few nm from their starting positions by a constrained optimization. The constraints ensure that the control does not stray far from the starting position during gradient calculations performed by dithering each segment. After tuning, the WFE is < 20 nm RMS. Immediately following this, a $1/2$ -wave shift is imposed by moving each MMA segment in piston only, inverting the pupil image from dark to bright. Multiple iterations of tuning and inversion are used to drive the pupil as bright as possible.

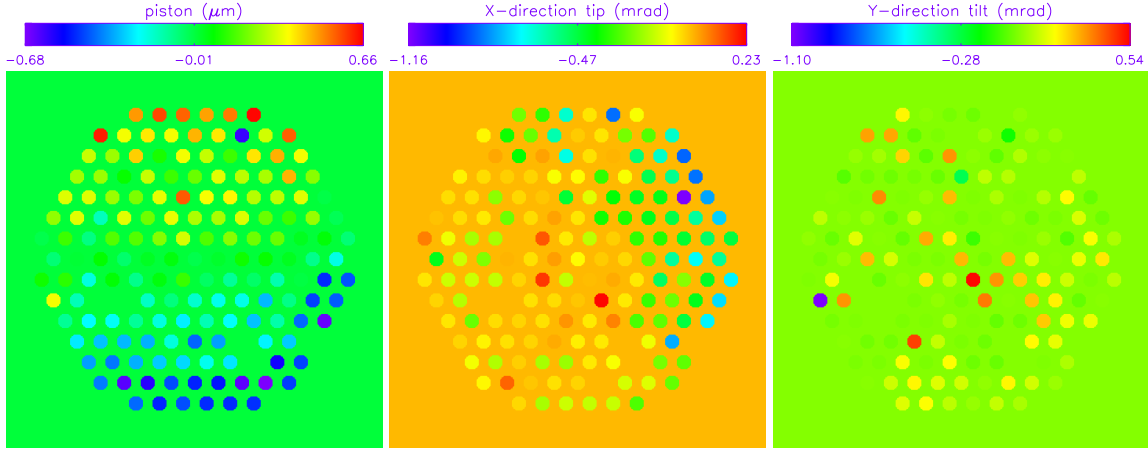


Figure 8: A flattened MMA state vector following application of Algorithms (2-5). The outlier segments are either due to unequal response, being off by a fringe, or a combination of both. The segment that appears as an outlier in yellow in the piston plot on the left is and the Y-direction tilt plot is one such segment that began exhibiting limiting behavior late in this effort.

6: Dark Channel Control

Up to this point the control has been entirely accomplished using only the images from the pupil camera and results in a wavefront error of < 20 nm RMS and a mean wavefront error of < 6 nm and the core of the PSF has been reduced by $\sim 10^4$. At this point fine modal control takes over. This operates by recognizing that only a limited number of control modes are needed to control most of the power within the dark -hole region. The number of control modes is incrementally stepped up to the full 200 that are pre-calculated, reaching progressively higher contrasts.[7, 8]. In general, the number of MMA mode settings are reduced through definition of an orthogonal control basis. The number of basis vectors is reduced by defining a region or patch of the focal plane where high contrast is desired. The response of the electric field for each basis vector (eigenvalues) is calculated and sorted according to eigenvalue in descending order. Only basis vectors (eigenmodes) that give appreciable gain are used. Modes that give little gain generally affect the result at or below the noise floor, i.e., the noise floor defines where the eigenvalues are cut off. Some of the lower order modes for a region extending from $15\lambda/D$ are shown in step (6) in Fig. 5. Fig. 2 shows the first 10 control modes of the 200 modes generated to achieve the milestone.

The dark channel control algorithm feeds back to update the MMA and PZT piston mechanism. The updates are calculated both for of these fine control devices using a set of constraints to maintain a temporally filtered zero mean MMA piston (averaged over the set of MMA segments), and shifting this low-frequency filtered mean piston to the fine delay PZT mechanism at lower bandwidth. MMA control voltages map \sim quadratically to MMA motion and this is included in the control algorithm. All control algorithms are performed at the same spectral bandpass and with the same images used to calculate the contrast.

7: High Contrast Image

Performing steps (1-6) result in a high contrast image, and starting “from scratch” for each DCE shows that the approach is stable and repeatable.

3.4 Milestone Validation Procedure

As established with the TAC, the procedure for the milestone demonstration is as follows:

1. The MMA is set to scratch, i.e., shutdown and power recycled, and the wavefront control system software is also restarted.
2. Wavefront control is performed in a cascaded and iterative manner to converge MMA actuator driver voltages that give an acceptable high-contrast wavefront solution for the targeted region of the dark channel detector. This has typically taken approximately three hours, starting from scratch.
3. When contrast in the dark zone stops improving, the high-contrast measurement begins while the wavefront control iterations are being performed, as described below:
 - (a) Wavefront control iterations are continuously performed at ~ 60 Hz sampling with a step frequency of ~ 6 Hz. This attempts to optimize the dark hole contrast in the specified region (the red region of Fig. 4).
 - (b) For each wavefront control iteration, one measurement is acquired with the best DM shape for high-contrast (no additional deformation on the DM to probe speckles). This measurement is used toward contrast measurement and toward the next control step.

4 Success Criteria

The required elements of the milestone are as follows: Each element includes a brief rationale.

4.1 Spectral Bandpass

A baseline spectral filter of 40 nm FWHM centered on 633 nm will be used. This filter will be calibrated with a lab spectrophotometer to measure its transmittance at 1 nm resolution. The baseline filter shall serve as the reference filter for future measurements.

Rationale: This filter will correct for spectral variations in the sources supercontinuum light. This is an issue that will not be encountered with real stars in a space mission.

4.2 Contrast

A mean contrast metric of 1×10^{-9} or smaller shall be achieved in a region extending from 1.5 to $2.5\lambda/D$, centered on $2\lambda/D$ in the focal plane for a spectral filter of 40 nm FWHM.

Rationale: This provides evidence that the high contrast field is sufficiently dark (10^{-9} expected exozodi level) to be useful for searching planets, and test whether there is a fundamental limitation at the inner working angle.

4.3 Confidence

Criterion 4.2, averaged over each of the three data sets (DCEs), shall be met with a confidence of 90% or better. Sufficient data will be taken to justify this statistical confidence.

Rationale: Assuming the contrast values have a Gaussian distribution about the mean contrast, this demonstrates a statistical confidence of 90% that the mean contrast goal has been reached.

4.4 Repeatability

Elements 4.1-4.3 must be satisfied on three separate occasions with a reset of the wavefront control system software (MMA set to scratch) between each demonstration.

Rationale: This provides evidence of the repeatability of the contrast demonstration. The wavefront control system software reset between data sets ensures that the three data sets can be considered as independent and do not represent an unusually good configuration that cannot be reproduced. For each demonstration, the MMA will begin from a "scratch" setting and the algorithm used to converge will have no memory of settings used for prior demonstrations. There is no time requirement for the demonstrations, other than the time required to meet the statistics stipulated in the success criteria. There is no required interval between demonstrations; subsequent demonstrations can begin as soon as prior demonstrations have ended. There is also no requirement to turn off power, open the vacuum tank, or delete data relevant for the calibration of the MMA influence function.

5 Demonstration Narrative

The key to broadband operation of the Visible Nulling Coronagraph (VNC) is achieving a condition of quasi-achromatic destructive interference between combined beams. Here we present efforts towards meeting this goal using Fresnel rhombs in each interferometric arm as orthogonally aligned half wave phase retarders. The milestone goal of the demonstration was to achieve 1×10^{-9} contrast at $2\lambda/D$ over a 40 nm bandpass centered at 633 nm. Rhombs have been designed and fabricated, and a multi-step approach to alignment using coarse positioners to get within range of piezo stages used for fine positioning of each rhomb in a pair and pair of rhombs relative to one another and the instrument. The previously demonstrated narrowband VNC sensing and control approach that used the same MMA in this effort is being adapted to broadband to include fine positioning of the piezo-mounted Fresnel rhomb APS. The goal was to demonstrate all of this in a low-pressure environment (< 0.01 atm). Ultimately, performance comparable to what was achieved in Milestone #1 was not achieved. Consequently, vacuum operation was not justified.

5.1 Design, procurement, and installation of achromatic phase shifters (APS)

Several analytical and tolerance modeling efforts have been presented on the use of Fresnel rhombs with coated and uncoated total internal reflection (TIR) surfaces to enable broadband retardance with minimal chromatic dependency.[17, 18, 10, 19, 11] Recent studies were performed to identify a coated TIR surface Fresnel rhomb solution using Lithosil fused silica[19, 11]. In theory, this approach can be used to achieve an arbitrarily broad high-contrast enabling retardance profile using glass with the highest-degree of transmissive homogeneity, but the feasibility of achieving the layer thickness tolerances for the chosen coating solution that provided the best performance with the least complexity was found to be beyond the state of the art of deposition control techniques. However, it was determined that conventional uncoated TIR surfaces with grade H4 BK7 could meet the demonstration requirements (see Fig. 9), and this is the approach that was pursued in this effort.

Using the theory presented in Sec. 2, the left panel of Fig. 9 plots TIR retardance as a function AOI derived from Fresnel equations for the central demonstration wavelength of 633 nm. Assumptions in this plot include Sellmeier dispersion for grade H4 BK7 in vacuum at room temperature. These conditions result in an AOI of $55^{\circ}4'48.5''$. While the determination of the design AOI was based on a vacuum medium, this demonstration is performed in air at pressures ranging from 1.0% to 100% atmosphere. The varying pressures at which the instrument is tested results in a slight shift in wavelength where the half wave retardance occurs. The important metric of overall RMS variation over the design bandpass is only marginally compromised.

The central panel of Fig. 9 shows the change in retardance as a function of wavelength over the targeted 613-653 nm demonstration bandpass at the standard AOI and atmospheric pressure. Additionally, curves are presented that represent ± 10 arcsec perturbations that are characteristic of residual error following coarse alignment. The associated leakage curves across the demonstration bandpass is plotted in the right panel

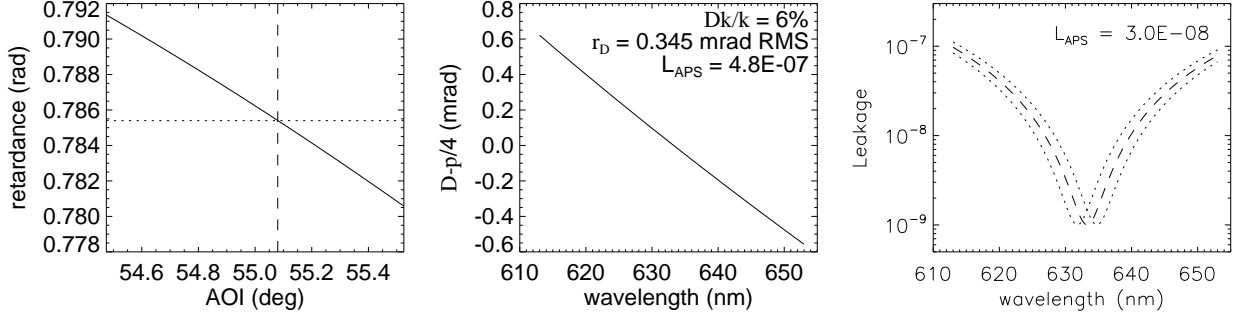


Figure 9: VNC Fresnel rhomb APS retardance curves - *left*: the AOI that gives $\pi/4$ retardance at 633 nm based on Sellmeier coefficients for BK7 at 1 atm and 293 K; *center*: change in retardance across the design bandpass at the nominal AOI (dashed) enveloped by ± 10 arcsec p-plane alignment or TIR surface parallelism errors (dotted line); *right*: Corresponding chromaticity of the null attributed solely to the slope of the Fresnel rhomb retardance for the ideal (dashed) and 10 arcsec perturbations (dotted).

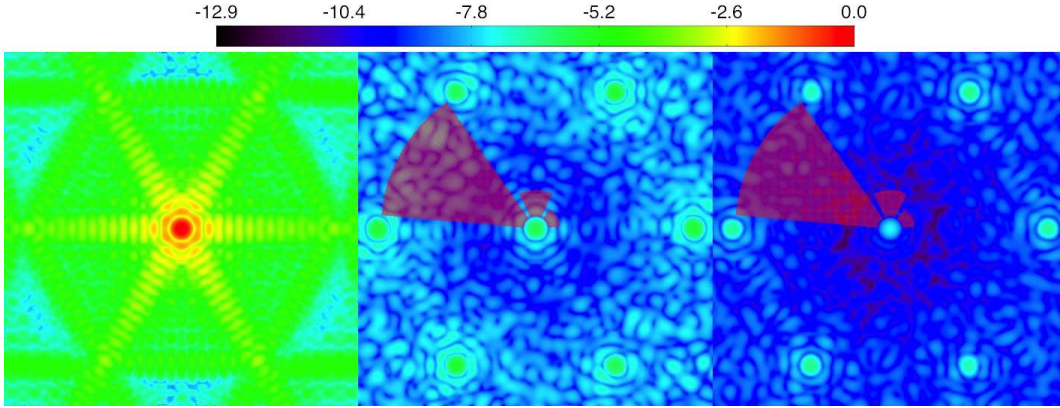


Figure 10: Log-scale normalized dark channel focal plane intensity of (*left*) the unsuppressed PSF, (*center*) the suppressed PSF with $\sigma_\delta = 345 \mu\text{rad RMS}$ per TIR and 3 nm RMS residual DM surface errors, and (*right*) the suppressed PSF assuming $\sigma_\delta = 1.17 \mu\text{rad RMS}$ per TIR and 3 nm RMS residual DM surface errors. Contrast statistics within each of the superimposed wedge-shaped regions are presented in Tab. 1.

Table 1: Expected dark channel contrast statistics corresponding to regions shown in Fig. 10.

	σ_δ	345 μrad			1.17 μrad		
	σ_{DM}	3.0 nm			1.0 nm		
	OWA [λ/D]	16	4.0	2.5	16	4.0	2.5
maximum		7.6^{-8}	3.4^{-8}	2.9^{-8}	1.2^{-8}	8.6^{-10}	2.9^{-10}
minimum		2.2^{-11}	1.6^{-10}	6.6^{-10}	1.5^{-12}	8.9^{-12}	2.9^{-11}
median		2.7^{-9}	3.4^{-9}	9.8^{-9}	3.5^{-10}	9.7^{-11}	2.0^{-10}
mean		5.6^{-9}	6.4^{-9}	1.2^{-8}	6.5^{-10}	1.8^{-10}	3.3^{-10}
RMS		7.3^{-9}	7.3^{-9}	8.3^{-9}	9.2^{-10}	2.0^{-10}	2.2^{-10}

of Fig. 9 illustrating null chromaticity. A leakage floor has been added to de-emphasize the $\pi/4$ intersection that analytically equates to infinite suppression. Note that the off-axis contrast is better than the 3.0×10^{-8} chromatic leakage suppression limit attributed to the $\sigma_\delta = 0.345 \text{ mrad RMS}$ retardance error of the APS. Off-axis contrast is shown in Fig. 10 incorporating the APS chromatic leakage and MMA segment surface errors. In practice, other limits to fabrication and alignment precision give rise to asymmetric spatial

and chromatic effects that raise the suppression floor. Here a floor of 10^{-9} is shown. A 2015 conference proceedings paper[20] presents a detailed description of the rhomb design process including geometric and coating tolerancing is presented along with the procedure used to integrate the full set of Fresnel rhomb APS into the VNC.

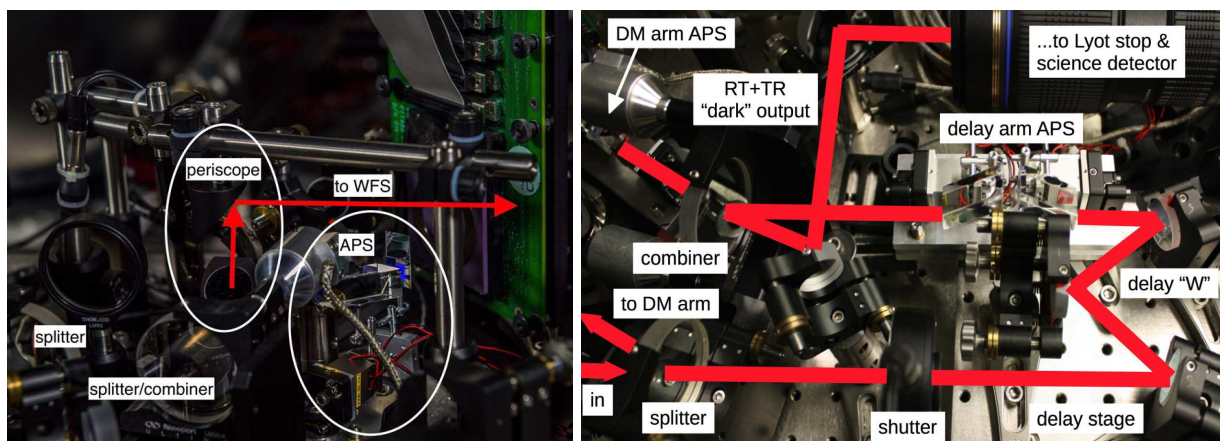


Figure 11: *Left:* The MMA arm Fresnel rhomb pair and bright periscope. *Right:* The delay arm Fresnel rhombs shown on their manual coarse and piezo fine stages, which are mounted on a common platform that enables alignment relative to the instrument and orthogonality to the MMA arm Fresnel rhomb pair. The beamsplitter and beamsplitter/beam combiner are captured in each photo from different angles.

The design and integration of the APS is described in proceedings papers.[11, 20] The design and redesign phase of the optics took place over the first half of 2014, and an order for two sets of symmetric, uncoated Fresnel rhomb APS was placed in the end of August 2014. The projected delivery date for the optics was to be the end of December 2014, however, fabrication delays pushed the delivery back to mid April 2015. During this time, low-cost COTS Fresnel rhombs were procured and used to design and test the hybrid coarse/fine alignment mechanisms. The rhomb mounts were revised, procedures were developed for integrating the rhombs (optomechanically and electrically), and the rhomb control software was written while the demonstration-grade optics were being fabricated. Having performed all of this work during fabrication, the demonstration APS were integrated within the VNC within two weeks following their delivery. The rhombs are shown integrated in the VNC in Fig. 11.

5.2 Dark channel detector upgrade

The narrowband VNC demonstration made use of a 12-bit CMOS detectors with a USB interface for both the bright output wavefront sensor and measuring contrast in the dark output. Since then, the dark channel detector has been upgraded to a low-noise (see Fig. 12 and statistics provided in Tab. 2) and higher frame rate 16-bit sCMOS detector with the aim of improving contrast and reducing the time required to reach the targeted contrast described in Sec. 6. The use of an EMCCD was explored in TDEM #1 and erroneously reported to have been used to reach the Milestone goals as described in that effort's Final Report. Ultimately, use of the EMCCD was curtailed due to a combination of issues with detector cooling, RF noise, and charge blooming in the focal plane, resulting in reverting to using the same model 12-bit CMOS detectors in both the bright and dark outputs, which do not require cooling.

The theoretical improvement to contrast sensitivity enabled by upgrading detectors is summarized in Tab. 3. Equivalent peak PSF starting contrasts (attributed solely to residual DM surface errors) are associated with different starting pixel values (in ADU) set to 80% of the detector full well. The dynamic range determined by bit-depth and noise properties of the detectors used in Milestone #1 (MS#1) and Milestone #2 (MS#2) yield different initial contrast values, contrast values following a single realization, and final achievable contrasts. Environmental noise, thermal drifts, and control actuation errors add noise to the measurement of wavefront error, thereby limiting correction and raising the contrast floor. The detectable contrast floor

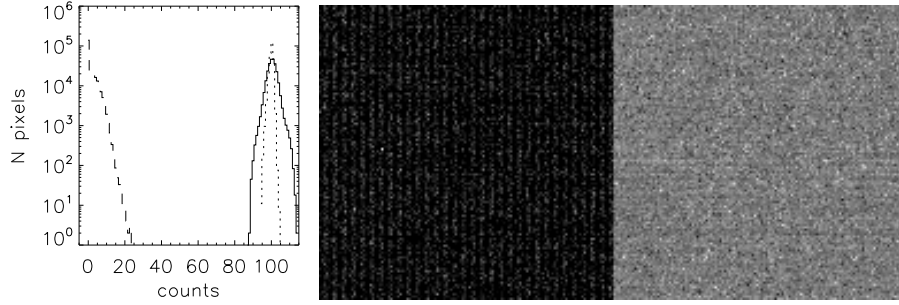


Figure 12: *Left*: histograms of detector bias frame data for the bright (dashed) and dark channel detectors (solid and dotted). The narrowband VNC TDEM used two of the same detectors, both being the same as what is still used as the bright channel WFS. The respective bright (central panel) and dark (right panel) single frame, and averaged dark frame pixel statistics are presented in Tab. 2

Table 2: VNC detector bias frame statistics. All units are in ADU.

	Bright (1 frame)	Dark (1 frame)	Dark (Averaged)
maximum	28	114	105.758
minimum	0	87	94.297
median	0	100	100.656
mean	1.835	100.453	100.540
standard deviation	2.6520	2.5412	0.8985

can be improved by allowing the core to saturate and instead using unsaturated average sidelobe intensity along with the core to sidelobe intensity ratio as a reference.

Table 3: Detector-limited (disturbance free environment, errorless actuation) contrast performance summary.

parameter	symbol	unit	MS#1	MS#2	notes
gain	g	e^-/ADU	1.0	0.5	
read noise	σ_r	e^- RMS	4.1	1.1	vendor specifications
80% full well (approx.)	fw80	ADU	3300	40000	
peak PSF core contrast	C_0	-	8.4×10^{-4}	8.4×10^{-4}	$\sigma_{DM} = 3$ nm equivalency
Initial contrast	C_i	-	1.24×10^{-5}	4.29×10^{-6}	at $2\lambda/D$
First realization contrast	C_1	-	2.91×10^{-8}	2.05×10^{-9}	at $2\lambda/D$
Final contrast	C_f	-	2.52×10^{-8}	8.82×10^{-11}	at $2\lambda/D$

The steps required to incorporate the new sCMOS detector for higher dark channel performance are described below.

Software development

The narrowband demonstration used two very similar CMOS of the same make, which simplified the software interface as both detectors used the same software development kit (SDK). The push for increased dark output performance (lower noise at higher readout rates) motivated pursuing an upgrade to an sCMOS detector with a CameraLink interface. Incorporating a detector interface using the SDK took longer than anticipated. Eventually, a set of initialization commands was identified that achieved the desired detector settings. Incomplete documentation of legacy and obsolete or conflicting command priorities complicated the process of achieving the desired detector gains, read modes, and pixel readout rates. Multithreading

with the bright channel WFS (a CMOS detector with a USB interface) and its different data format gave rise to display syncing errors. The display syncing issue was tolerated until a bug was eventually identified and eliminated shortly after identifying a specialist that addressed the issue in short time.

Vacuum cable fabrication

In order to reach higher contrast and demonstrate component functionality in a low-pressure environment, the VNC optics and detectors are placed inside of a vacuum chamber, whereupon it is referred to as the Vacuum Nuller Testbed (VNT). The control computer and amplifier electronics remain outside the chamber. Flanges and feedthroughs have been added to the system to accommodate leads needed for both the APS fine positioning piezos and the new sCMOS detector. The first attempt at making a hermetic passthrough for the CameraLink cable (see Fig. 13) used a potting approach to maintain cable continuity and limit the potential of introducing environmental noise, ground-loops, and impedance matching issues.



Figure 13: From left to right: the first CameraLink passthrough, installed on the VNT, the two cable assemblies (foreground are a pair of vacuum and air-side cables), in-air testing of the HD44 connectorized cables, and the HD44 flange and adapters prior to installation on the 6-way cross added to the VNT chamber for the broadband demonstration.

It was determined that the potted passthrough leaked at a rate that limited off-pump operation below the targeted 1% atmosphere level to only 40 minutes. Separating the CameraLink cable into air-side and vacuum-side cables using an HD44 bulkhead vacuum interface was suggested as a path forward. The necessary hardware was procured along with additional adapters and fittings to replace the leaky passthrough cable. The second spare vacuum CameraLink cable acquired at the same time as the cable used for the potted passthrough was cut and re-connectorized with HD44 hardware. The cable assembly was tested in air independent of the flange, which was tested for leaks before testing the cable across the flange. The effort was successful at eliminating the vacuum leak with a cable assembly that maintained performance characteristics of a continuous cable.

Cooling

The dark channel sCMOS detector is built with a thermoelectric cooler (TEC) to minimize thermal noise (dark current). Heat removed by the TEC is passed to a heat sink, which radiates away heat and in addition to being optionally air-cooled by a fan, or using flowing water. Flowing water through the heat sink is preferred since the fan introduces mechanical noise and air currents during operation at atmosphere, and does not cool when operating at low pressure (there is insufficient air to blow and cool the heat sink). A chiller with a mechanical pump is used to circulate water through roughly 60 feet of tubing across the lab and into the vacuum chamber (see Fig. 14).

In the initial buildup of this system, a fail-safe condition was triggering the fan to switch on after only minutes of acquisition, indicating that the detector was not being adequately cooled. It was determined that the first chiller that was used had a non-functional cooler and the pump was not maintaining adequate flow through the long lines of plumbing to the detector. The chiller was replaced with a second unit with a functioning cooler and a higher output. The system is now streamlined and the flow rate in the system is maintained at half of what is recommended by the camera manufacturer to reduce fluid turbulence, and

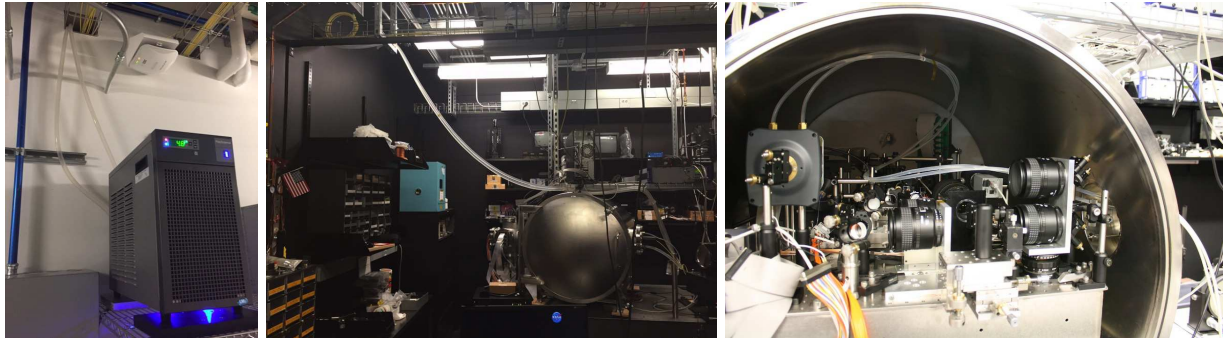


Figure 14: Chiller and water lines to the sCMOS detector inside the VNT. The water lines cool the detector’s thermo-electric cooler heatsink during low noise and vacuum operation in place of the built-in fan that introduces vibrations and relies on the presence of air.

this has been adequate to not trigger the fan fail-safe during extended high frame rate operation.

5.3 Control rate adjustments

Based on prior experience in the narrowband Milestone #1, a complete DCE event consists of hundreds of thousands of images from the dark focal channel detector that previously was readout limited at ~ 40 fps and has been upgraded in this demonstration, now approaching ~ 70 frames per second readout. The lower noise of this detector should both reduce the number of required images, and, paired with the faster frame readout, the amount of time required to reach an equivalent contrast reached in Milestone #1. The goal in this Milestone was to improve contrast by $> 5\times$ over a $\sim 33.3\times$ broader spectral bandwidth compared to the previous narrowband effort, and this goal was not met.

The VNC, its source, and the demonstration filter require an exposure time of ~ 10 ms needed to reach 80% full well of the dark sCMOS detector, for which the maximum frame readout is 69.8 fps in 16-bit resolution mode. During fine null control, the sub-steps of computation, printing out calculated contrast in the control interface, and saving frames to disk results in a fine control step rate of 5.8 per second. The added overhead of printing out the contrast and saving frames is negligible compared to computation overhead – without these added processes, the null control rate is only improved to 5.9 steps per second. The polynomial-based ARMA model used by the control software defines the weights and averaging process for the current frame plus a weighted sum of previous frames. Each DCE would consist of a total of hundreds of thousands of frames of which only the last several tens of thousands of ARMA frames would be stored as disk FITS files to analyze and calculate contrast.

Each progressive DCE would be separated by > 12 hours from the previous DCE. The narrowband demonstration used the first $\sim 50,000$ images to construct the shape of the dark hole and achieve successively better contrast. After this approximate number of images the system was observed to have converged and contrast was stabilized. The last 3,800 recorded images were the best in terms of contrast and stability, and it was these images that were retained and archived and used to report the contrast metric. This set of 3,800 images represented ~ 950 seconds of data. The same performance was not achieved in this broadband effort. There were and are 200 control modes being used in the demonstrations (the first ten of which are shown in Fig. 2), and each control mode is sequentially stepped starting with the mode of greatest influence inside the high-contrast region of interest and continuing to mode 200, which produces the least amount of influence.

The Milestone goals are based on the statistical ensemble of multiple contrast realizations per DCE. This metric is what is important for a flight coronagraph that runs WFC in closed-loop, since flight missions are likely to be photon-starved for the exoplanet and would likely require significant averaging to detect an exoplanet.

5.4 Full-yield segmented DM testing

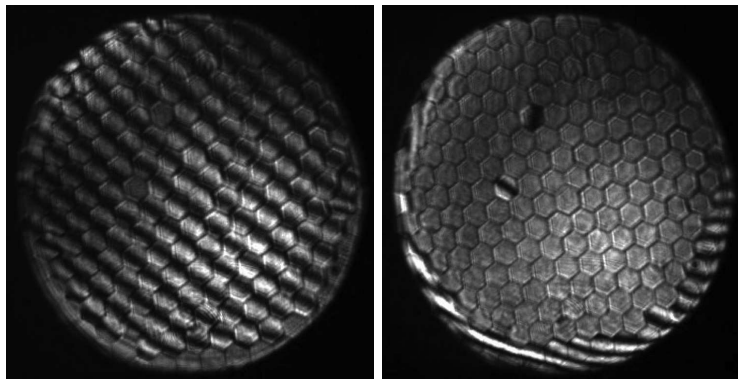


Figure 15: The full yield Iris, AO PTT489 that was installed in the VNC and in use briefly before two segments became inoperative. An attempt made by Iris, AO to recover use of these segments resulted in irreversible damage to the device, at which point the decision was made to revert to using the TDEM #1 MMA.

A full-yield (all segments active with three degrees of freedom) Iris AO, Inc. PTT489 MMA was installed in the VNC in late spring 2015 and in use briefly before two segments became inoperative (see Fig. 15). The device was returned to Iris AO to attempt to recover use of these segments. Unfortunately, however, this attempt at repair resulted in unexpected irreversible damage, at which point the decision was made to revert to using the TDEM #1 MMA, which has proven reliability. The switch back to the heritage device was done in late June of 2015. Another full-yield MMA remains in reserve in the VNC lab for use in future demonstrations with an upgraded system (see Sec. 6.1)

5.5 Filter bandpass measurements and source characteristics

One of the Success Criteria (Sec. 4) that was met was to measure the transmittance of the 40 nm baseline filter centered at 633 nm (Sec. 4.1). This filter was measured along with four others intended for coarse and fine phasing steps and to characterize bandpass-dependent performance of the VNC with the APS. Plots of the in- and out-of-band transmission measurements for these filters are shown in Fig. 16.

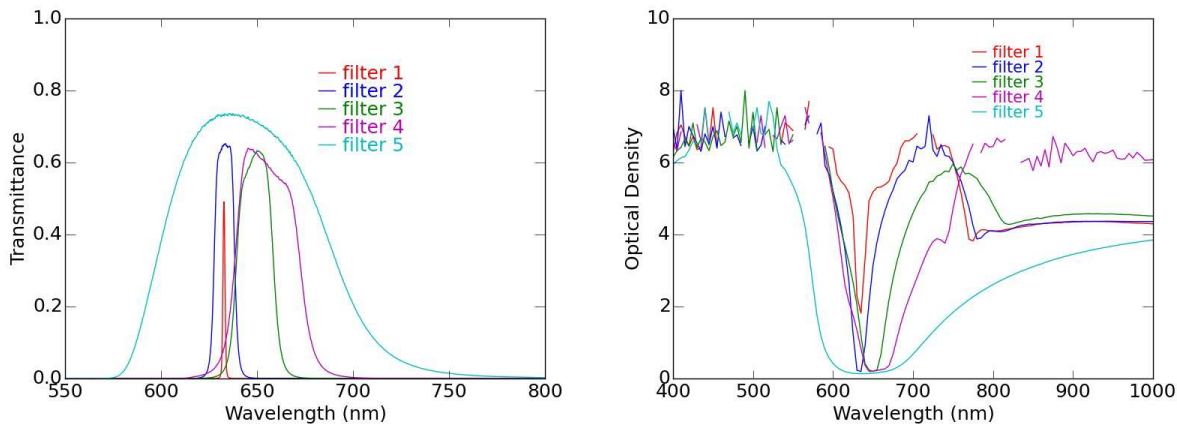


Figure 16: Measured VNC filter set transmission and optical density. Filter characteristics are summarized in Tab. 4.

Filter 4 was measured to have characteristics that most closely matched the proposed Milestone bandpass. Filter 5 has the shortest coherence length, and was therefore the most useful for locating the central fringe when phasing the MMA as shown in Fig. 7. The supercontinuum source spectral density is relatively flat 0.07 mW/nm between 600–700 nm, falling off steeply shortwards of 600 nm approaching zero output at 440 nm. The fiber into which the supercontinuum source is coupled following filtering has a single mode cutoff wavelength < 600 nm.

Table 4: VNC filter characteristics as measured by spectrophotometer

filter	λ (nm)	FWHM (nm)	$\Delta\lambda/\lambda$ (%)	$\lambda^2/\Delta\lambda$ (waves)
1	632.8	1.26	0.20	502
2	633.1	9.64	1.52	66
3	649.2	17.5	2.70	37
4	654.7	31.7	4.84	21
5	643.9	80.3	12.5	8

5.6 Vacuum leak rates and outgassing tests

An experiment was performed to characterize the potential for mount and zoom lens virtual leaks and outgassing issues that would coat the surfaces of the custom polarization optics-based APS and MMA. The experiment consisted of pumping down the VNT chamber to ~ 140 mtorr, which takes an hour using the combination dry drag and turbo pump and the system leak and virtual leak rates. Efforts were successfully carried out to reduce leak rates from ~ 0.2 torr/min, which would limit < 0.01 atm operation to 40 minutes with the pumps switched off, to a rate that maintains the < 0.01 atm condition overnight.

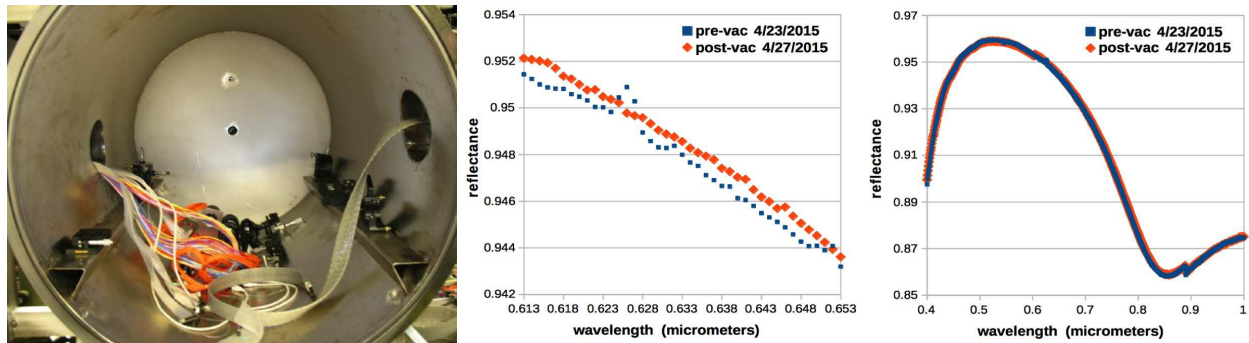


Figure 17: The vacuum test performed to check for potential outgassing of mounts and zoom lenses that are not designed to be vacuum compatible performed to address concerns that greases in these mechanisms might coat the surfaces of the custom polarization optics and MMA. The reflectance of a witness sample was measured with a spectrophotometer before and after a 67 hour period sharing the chamber with components similar to those used on the VNC breadboard.

The reflectance of a witness sample was measured with a spectrophotometer before and after a 67 hour period with the surface exposed in the chamber at 220 mtorr with 4 zoom lenses and 19 mechanical mounts similar to those used on the VNC breadboard providing traceability as sources of outgassing. The data shown in Fig. 17 suggests that operation through several high-contrast demonstration runs at < 1 atm pressure does not present a significant risk of coating the key custom optical component surfaces of the VNC, most importantly the MMA, beamsplitters, and APS.

5.7 Stability measurements

VNC stability was measured to characterize the ensemble influence of source brightness fluctuations, acoustical and mechanical perturbances, and electrical noise in control amplifiers, and thermal drifts, all of which add time to the VNC method of high-contrast WFS/C, which is to control through observation using an increasing number of control modes with decreasing amplitude using an ARMA approach. The WFS bandwidth and sensitivity paired with the WFC elements' stroke and bandwidth coupled with the ability to offload large low spatial frequency modes limit the amplitude and temporal frequency cutoffs that can be compensated. Generally speaking, while the ARMA approach to control can damp out large amplitude

impulses or average through sustained small amplitude vibrations, a more stable system will reach higher contrasts faster.

System instability was measured by quantifying the change in photon counts in a square region of interest of the bright output detector within a flattened MMA segment on a “grey” fringe where response is linear between a constructive and destructive interference peak. Instabilities attributed to source brightness fluctuations are quantified by closing the MMA arm shutter and repeating the measurement in the same region of interest.

Fig. 18 presents an example stability measurement before and after reinforcement of a suspended rack that holds the VNC control computer and amplifier electronics. The labels “prebrace” and “postbrace” for the two curves in each plot of Fig. 18 reference measurements made with the system before and after adding the reinforcements. The racks support the VNC control computer and amplifier electronics above the VNT, which itself rests on a pneumatically-isolated table. Cables running from the control electronics to the chamber introduce a mechanical short-circuit that transmits vibrations.

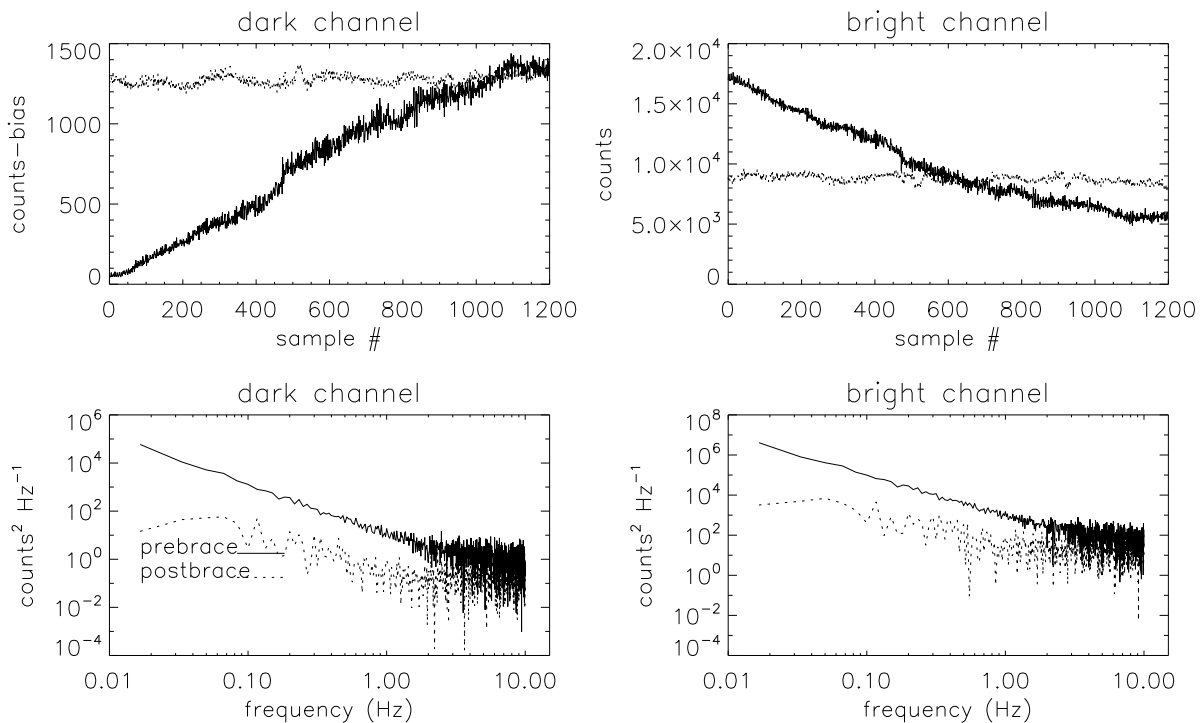


Figure 18: Sample time series and power spectra of photoelectron count variations due to environmental disturbances and source fluctuations averaged over 6x6 pixel square ROI on the detectors in each output of the VNC with the system at rest. The system is at rest during data acquisition.

The sample data shown in Fig. 18 is just one example change in condition that was measured to check for sources of and improvements to stability. It is noted that in this data set the long period drift is not likely to be associated with the rack sway mode perturbation that was under test pre- and post-reinforcement. The data do indicate an overall improvement in stability as observed with the 1–2 order of magnitude shift in the power spectrum, however, the observed slow drift can more likely be attributed to delay optics settling following coarse phasing.

Another example variable that was considered was the time of day when the system was operated, the hypothesis being that the system operates under more stable conditions at night when, e.g. foot traffic and doors opening and closing throughout the building are at a minimum. Data were recorded at 8PM and 1PM

on a Monday and Tuesday, respectively. Surprisingly, the midday data produced a more stable measurement than the evening data.

Ultimately, no closed-loop stabilization data have been generated for this demonstration to be compared with similar data in the narrowband Milestone #1. This remains a work in progress.

6 Results and lessons learned

We were unable to close the loop on broadband control in this effort and therefore no contrast maps are included in this report.

6.1 Known issues to be addressed in future efforts

Known issues that have been identified as being hindrances to reaching the broadband Milestone in this effort are described below and summarized in Tab. 5. Addressing these issues will be carried out pending continued funding through, e.g., SAT/TDEM and/or GSFC IRAD awards.

Mount instabilities

While it has been the claim that one of the major advantages of the VNC approach to WFC is observation through the control sequence, this relies on trades between control rates and the power spectrum of perturbances, which is a net sum of slow thermal and (induced) electrical drifts, as well as sustained and impulsive mechanical and acoustical disturbances. Careful attention to avoiding system resonances and/or the design of isolation and damping mechanisms can be used to offload sensitivity requirements.

Instabilities present in the breadboard VNC have prompted the need for realignments and alignment checks, followed by updating digital masks files, such as that which corresponds to the MMA control mode targeted high-contrast region over which contrast is calculated. On multiple occasions, the PSF has been observed to drift on the dark detector, which drastically reduces the efficacy of the control routine. An example is shown in Fig. 19, where over the course of one night with no known activity in the lab, the PSF was observed to shift by $\sim 1\lambda/D$ relative to a mask that had been generated the previous day.

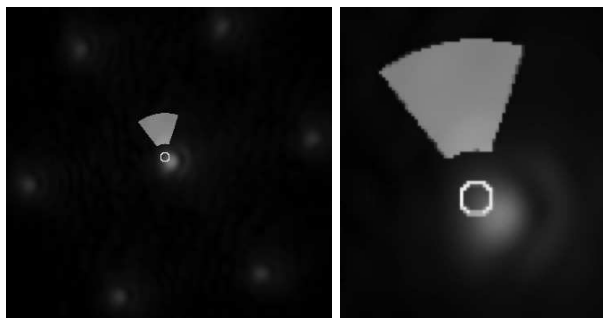


Figure 19: Analysis of the final attempt at closing the WFC loop revealed that the image had shifted on the dark detector, and therefore also relative to the predefined control mask. These figures show the location of the delay arm PSF (MMA shutter closed) relative to the location of the last measured center of the PSF for which the control mask had been generated. The $\sim 1\lambda/D$ diameter circle drawn on the data is centered on the last measured PSF center.

Adjustments to either the fore-optics or the delay line requires modifying or generating a new MMA lookup table “flats file.” The process of array phasing is not a new issue to the system, but acquiring a “feel” for this process is something that takes time for not just a new user, but also for each MMA and its calibrated controller. In practice, generating a flats file involves significant human-in the loop interaction that can sometimes converge quickly, or at other times be very time consuming. The goal is to mitigate instabilities such that the flattening of the DM can be as automatic a process as possible that needs less and less human-in-the-loop monitoring and intervention. Instability mitigating steps including simplifying the aft-optics and modifications to the vacuum chamber discussed in this section below will also serve to improve the system’s performance.

Table 5: Summary of issues listed by priority, highest first

Issue	Root Cause	System Effect	Mitigation Path
Mount instabilities and dark channel optics	Shifts and/or slow drift in e.g. DM mount, aft-optics frictionless zoom lenses, and 1/2" post-mounted components between measurements and after chamber loading following external alignment checks; an overly complicated imaging relay	Dark channel PSF shifting and Strehl degradation as well as chromatic aberration; reference beam tilt and path errors that can be observed on both bright and dark detectors, confounding coarse human-in-the-loop and automated fine control routines	Simplify aft-optics design, use more rugged mounts, and remove unneeded actuation – the aft-optics were redesigned in May 2016 and ruggedizing effort began in June 2016
Deformable Mirror	Amplifier to device calibration is suspected to have drifted, manifested by observed irregular (not flat) fringe pattern when the DM is set to zeroes	A subset of individual segments reach the limit of control or exhibit significant non-linear response during automated phasing and fine control	A fully-functional DM and its calibrated amplifier that have been held in reserve will be installed in the coming weeks; the DM and amplifier that have been used will be recalibrated for future use
Delay stage	Backlash error in absolute stage positioning on the order of 1–2 μm is observed using both human-in-the loop stepping and automated fringe tracking; creep is suspected	While the stroke of the PZT used for fine actuation is adequate to compensate for absolute errors, slow creep may be a source of drift away from the central null fringe during fine controls	Quantify settle time wait period needed following coarse stepper actuation before attempting fine controls; explore incorporation of a hybrid slip-stick/PZT actuated coarse/fine delay mechanism
Vacuum chamber	A limited number of access ports necessitates a six-way cross that 1) encumbers cabling and 2) introduces a torque on the system and its passive isolation	Optical mounts are subject to being inadvertently bumped or snagged during cabling – alignment checks must in some cases be repeated external to the chamber; the torque mode introduces an unwanted resonance	Ports are to be added to the chamber in the coming weeks that will enable incorporation of a connector panel for robust cable harnessing with the added benefit of yielding a more symmetric isolator load
Achromatic phase shifters	Uncoated BK7 APS were selected for this demonstration following no-bids for multi-layer coating designs that yielded more favorable performance with a more high-purity glass option (Lithosil)	The theoretical retardance is marginally acceptable for meeting the Milestone goals, constituting a significant contribution to the leakage error budget	Fabricate a new set of APS with multiple orders of magnitude improved theoretical performance consisting of rhombs with single layer coatings on the TIR surfaces within fabrication capability; the design may enable a simplified approach to mounting that improves stability
Control OS	The Windows XP OS that has been in use exhibits bus issues and does not guarantee latency of computer operations	Communications with detectors and amplifiers periodically fail at initialization or are lost during operation and must be reset; control bandwidth is compromised	Work has begun on migrating to a system with 16 processor cores and 32 processor threads running a Linux kernel in hard realtime
Fiber bundle array	Anamorphic pitch mismatch between fiber bundle arrays and their segmented DM counterpart has proven to be a difficult problem to address optically, requiring complicated relay schemes; transmission properties have yet to be characterized adequately to justify the added complexity needed for their incorporation	Complex wavefront control is performed with the DM alone, leaving segment figure errors uncorrected and no means for fine amplitude control	Characterization of several FBAs has been proposed as work to be performed in parallel to upcoming VNC efforts; if a candidate component is identified, a vacuum-compatible optical relay will be designed for their incorporation with the system

Dark channel optics

The dark channel aft-optics relaying the MMA pupil to the Lyot mask to the focal plane have proven detrimental to achieving the VNC broadband Milestone. The aft-optics include several zoom lenses, the

justification for which was to match the segment spacing of the MMA to the pitch between fibers in a single mode spatial filter fiber bundle array (FBA). The FBA is meant to enable complex (phase and amplitude) WFC as a passive unit, thereby enabling deeper contrasts and/or access to more discovery space in the image plane. The alternative approach to yielding comparable control is to use two DMs (not necessarily MMAs), one in a pupil, the other in an intermediate optical plane to use the Talbot effect. The attractiveness of the FBA approach that has been pursued with interferometric efforts in the past is that it is a passive component (i.e., does not require an additional amplifier and numerous signal leads that require a proportionate increase in power and introduce added complexity and failure modes) that enables amplitude balancing by controlling each individual MMA segment's tip and tilt to fine tune coupling into it's corresponding fiber.

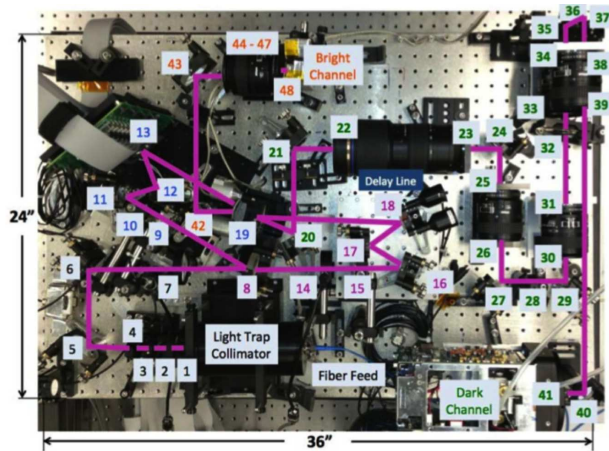


Figure 20: The left figure is from the VNC TDEM Milestone # 1 Final Report[8] showing the experiment breadboard layout. There were two additions made to the layout for this broadband effort: 1) the four Fresnel rhomb prisms that comprise the APS residing between elements 13 and 19, and 18 and 19 in the MMA, and delay arms of the interferometer, respectively, and 2) rotating fold mirror 42 out of plane and adding an additional mirror between this element and fold mirror 43 to periscope over the MMA arm Fresnel rhomb assembly

Simultaneously demonstrating FBA and APS capabilities has not been attempted in this effort. Instead of using an FBA, a Lyot mask was used to block the regions of non-overlap between the reference (delay) and MMA arms. The regions of non-overlap include the segment gaps, the perimeter around the MMA outermost hexagonal ring, and five non-functioning segments. Until a candidate FBA has been identified as one that could significantly improve system performance (contrast, throughput, or both), there is no requirement to match FBA and MMA spacing. This renders the aft-optics used in this demonstration as having been: 1) overly complicated, 2) sources of chromatic aberration (see Fig. 21), 3) sources of vacuum virtual leaks that give rise to outgassing concerns (Sec. 5.6), and 4) a complicating factor in achieving and maintaining alignment (Sec. 5.7). Fig. 20 shows the closest representation of the layout used to reach the narrowband VNC Milestone. Optics labeled 20 through 41 in the figure comprise the dark channel aft-optical system, including five zoom lenses, eight fold mirrors, a polarizer (28), the Lyot stop (32), a diverger lens (36), and the detector (41). Effects of chromatic aberration through the system are shown in Fig. 21.

Two designs have been modeled to simplify the aft-optical system, one being all reflective (suggested in July 2015), and one using achromatic doublet lenses generated in early 2016. The systems use 1:1 relays, which is all that is needed to further efforts toward reaching the projected broadband performance capability using a binary Lyot mask in place of the FBA. The designs eliminate the susceptibility to magnification errors introduced by the zoom lenses, as well as the aberrating and proneness to perturbation of the periscope comprised of optics 33-39. Once broadband performance is demonstrated and a FBA candidate is identified for testing, any redesign of the aft-optics needed to accommodate the FBA will be undertaken.

Fully-functional segmented DM

The Iris AO, Inc. PTT489 mirrors used by the VNC for wavefront control have improved. Previously these devices had many non-functioning segments. Now, fully active devices are being made. One such device was installed in the VNC to be used for the broadband demonstration. Two actuators became inoperative following several weeks of initial testing (see Fig. 15). Loss of control of these segments occurred during a week of high humidity and high temperature conditions resulting from facilities improvements shutting down the GSFC B34 HVAC environment control. It is not clear that the building and lab's high humidity and

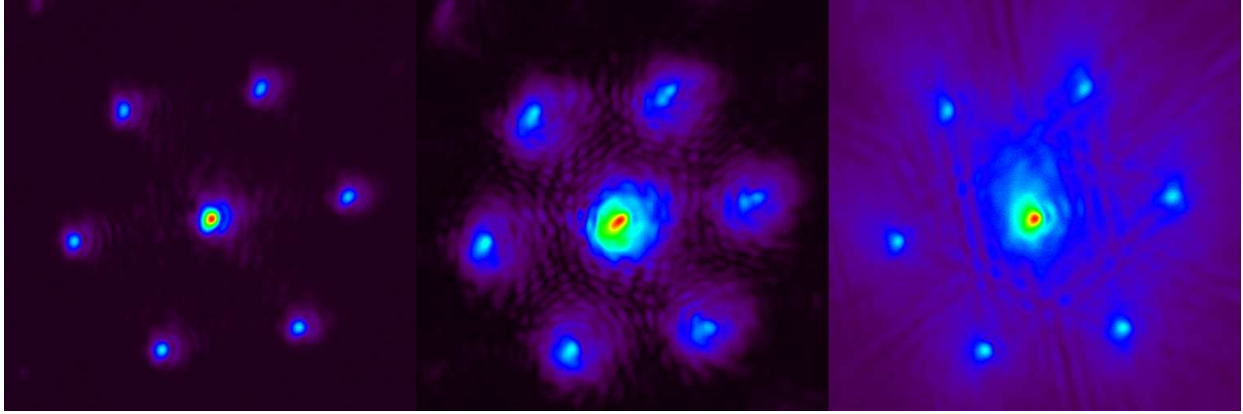


Figure 21: *From left to right*: single frame reference arm dark channel PSFs using a supercontinuum source with a 40 nm filter, an 80 nm filter, and without a filter. It is noted that the ~ 600 nm single mode fiber cutoff wavelength allows higher-order modes to enter the system and this adds to the effects of chromatic aberrations observed in the scatter background and spreading of the PSF core observed in the right frame included for illustrative purposes.

temperature contributed to the anomalous behavior, or if it was coincidence. The device was returned to Iris AO, Inc. along with its controller for servicing and recalibration. The effort was unsuccessful, and the decision was made to reinstall the device that was used to reach the narrowband milestone, which has five inactive segments, but otherwise has performed reliably. A replacement 100% yield DM of slightly poorer surface quality remains in reserve.

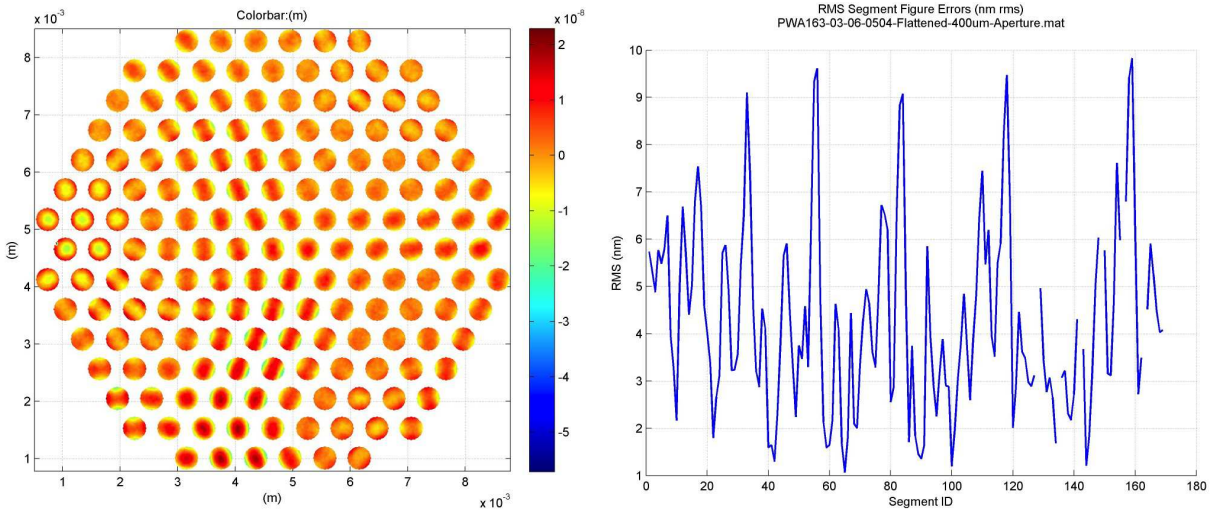


Figure 22: *Left*: Measured 400 μm circular subaperture surface data of the Iris, AO PTT489 DM used to reach the narrowband milestone[7]. This same DM is presently being used to begin work towards reaching the broadband milestone. Two out of five segments that are masked out by the Lyot stop are apparent, one as a missing segment, the other showing an astigmatic pattern. *Right*: A corresponding plot of the RMS surface error within each circular subaperture. An array of single mode fibers could be used to further reduce the correlated wavefront error over the low spatial frequencies corresponding to the dark region of highest contrast targeted by the wavefront control algorithm.[7, 8]

Delay stage

The VNC delay stage uses combined long-travel coarse stepping and 20 μm piezo-actuated linear drives. A magnet keeps the actuator stack coupled to the stage. Backlash error in absolute stage positioning on the order of 1–2 μm is observed using both human-in-the loop stepping, as well as an automated scanning approach to locate the central fringe as described in Sec. 3.3.

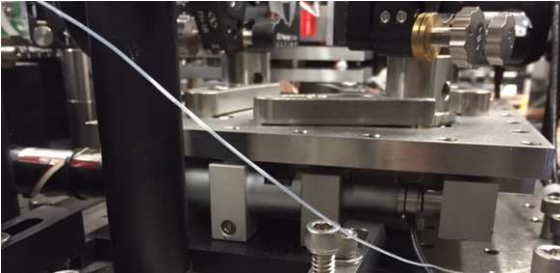


Figure 23: The VNC combined long-travel coarse stepping and 20 μm piezo-actuated linear drive delay stage. A magnet and preload are used to work against the actuators and minimize backlash. The stage presently holds the three mirrors and one pair of Fresnel rhombs comprising all optics in the delay arm excluding the polarizer and shutter used for amplitude balancing and calibration.

Improved routines, if not also an improved or streamlined hardware approach are needed to ensure that the delay stage is set to zero delay between arms to minimize consumption of MMA stroke, which can lead to out-of-range conditions for individual segments. Improving the delay mechanism will become more important as MMA or DM stroke is reduced in order to improve control resolution that is limited by amplifier resolution and environmental or system electrical noise properties. One possible approach is to eliminate the coarse stage, which is presently incorporated as a mechanism for enabling variable shearing to set the instrument IWA, or more generally, change the transmission pattern on the sky. Such a mechanism implies the need for multiple Lyot masks to accommodate different shear settings, and this further complicates the design. A fixed shear with a field rotator may ultimately prove to be the best method for achieving maximum on-sky discovery space.[12]

Vacuum chamber modifications

A limited number of access ports on the main chamber has necessitated use of a six-way cross that 1) encumbers cabling and 2) introduces a torque on the system and its passive isolation. Optical mounts are subject to being inadvertently bumped or snagged during cabling necessitating alignment checks that must in some cases be repeated external to the chamber. The torque mode introduces an unwanted resonance. Modifying the chamber by adding ports is will address these issues.

The VNT main chamber currently has two ports for all of the VNC electrical, optical, and fluid feedthroughs, the majority of which are passed through the six-way cross added for this effort (see Fig. 24), replacing a four-way cross used for the narrowband milestone. The two additional ports in the new cross are used to 1) interface the APS fine positioning PZTs with their amplifiers using BNCs, and 2) interface the sCMOS dark channel detector, which uses a custom modification to a vacuum CameraLink cable. The other feedthroughs that were used in the previous demonstration include potted circular connectors for USB cables wire bundles for, detectors, shutters, and delay stages, as well as potted rectangular connectors for the MMA. The requirement for this added cabling has increased the risk associated with moving the VNC in and out of the VNT chamber, which must be done periodically for system modifications and alignment checks. Alignment has been inadvertently perturbed while mating cables and connecting the dark detector cooling lines, and each transfer presents a risk of damaging an electrical lead, all of which are needed for full functionality of the instrument.

It is noted that additional pointing system bulkhead feedthroughs would eventually be needed for stabilizing a beam passing through a vacuum optical window relayed from an air-side system, e.g., an actively-controlled lab-scale segmented telescope used to demonstrate end-to-end sequential wavefront control before and internal to the VNC. A cost and lead-time quote has been obtained for adding ports to the chamber. It is expected that making these modifications will also improve system stability - the significant mass of the many flanges and bulkheads cantilevered off of the side of the chamber would be more symmetrically distributed about

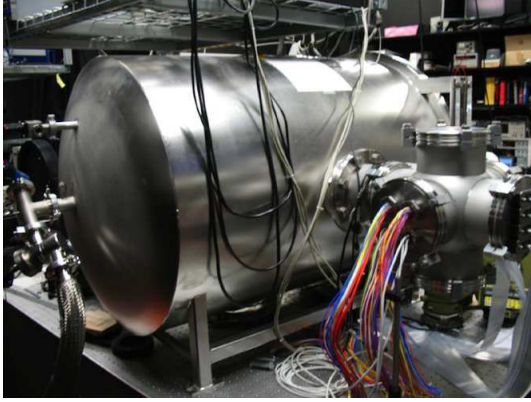


Figure 24: The VNT main chamber currently has two ports for all of the VNC electrical, optical, and fluid fluid feedthroughs, the majority of which are passed through the six-way cross added for this effort. Adding ports to the chamber will reduce the risk of damaging cables or perturbing instrument alignment, while also improving stability.

the chamber, thereby eliminating what presently introduces a resonant torque mode on the VNT and the dampers on which it rests.

A simplified coated Fresnel rhomb design

In theory, it may be possible to improve Fresnel rhomb APS performance using a single layer of magnesium fluoride deposited on fused silica rhombs to reduce the RMS retardance variation over a given bandpass[17, 18], or to design to broad bandpasses with compromised contrast. The advantage of this approach is that it can be measured with conventional thin film equipment. The coating layer can be deposited on a material with a high index of refraction, e.g., sapphire or SF11, in order to measure its thickness very accurately using ellipsometry. Once the film thickness and properties are characterized, it can be deposited on high grade (homogeneous) fused silica, again using a high index material as a witness for conventional characterization.

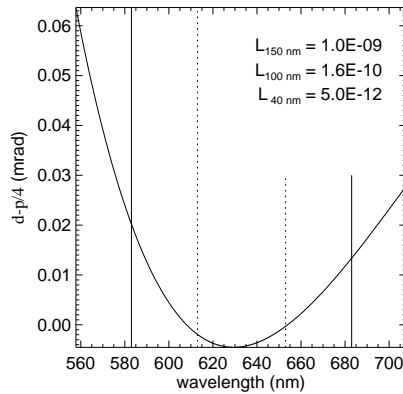


Figure 25: A BK7 APS using a single 12.7 nm thick MgF2 layer coated on each TIR surface using an AOI of 51.4723 degrees. Leakages are calculated for 150, 100, and 40 nm bandpasses.

Realtime operating system (RTOS) implementation to improve control cadence

The VNC control algorithms are implemented in C/C++ with threading in a Windows XP environment. Using Windows XP as the control OS has been problematic throughout this demonstration, primarily in maintaining consistent communication with the detectors and amplifiers needed for sensing and control. Cameras, mechanisms and the MMA are controlled through different threads. The Windows XP system will no longer be used in future VNC efforts. Iris AO has provided a Linux driver for the MMA and development of multi-threaded C message passing interface (MPI) control code using a Linux-based RTOS has begun. A near-term goal is to increase control rates from the current ~ 6 steps per second to > 100 steps per second. This will be accomplished by completing a port of the VNC control software from a standard Windows implementation on a single processor machine to a parallel processing system with 16 processor cores, 32 processor threads, with a real-time Linux kernel. At the time of writing this report, detector frame readout has been demonstrated with this machine using both CameraLink and USB 3.0 interfaces at rates of hundreds

of frames per second.

Fiber bundle array (FBA) testing

The Milestone #1 report stated a requirement for incorporating a single mode FBA in Milestone #2. Each fiber is optically mapped to one MMA segment and it functions as a passive wavefront corrector since wavefront errors at the spatial frequency scale of one cycle per MMA segment and higher are not coupled into the fiber but shows up a small coupling loss (throughput loss). The FBA is also meant to function in concert with the MMA to actively correct amplitude errors by adjusting tilt to affect the coupling overlap integral.

The FBA was a jointly-funded effort between GSFC and JPL. Both funded Fiberguide Industries to develop a test unit that was delivered to GSFC in June of 2010. Separate versions of the Fiberguide units were tested at both GSFC and JPL, and both reached the conclusion that the lenslet arrays were misaligned. JPL and GSFC worked with the vendor to rectify this problem and the JPL version has now been properly aligned and separately tested at JPL. The GSFC version previously underwent realignment at Fiberguide's facility.

No TDEM funding was used for recent FBA characterization efforts. A set of two Agilron FBAs from were delivered to GSFC in April 2015 under SBIR Phase II Contract NNX13CG04C. Restarting an effort to characterize these units for use in the VNC is a near-term goal that will be undertaken pending the availability of personnel capable of performing the task.

7 Milestone Certification Data Package

The broadband VNC Milestone was not met in this TDEM-10 effort, and the certification data package is therefore not available for review by the Exoplanet Exploration Program and its Technology Advisory Committee. The authors of this Report are aware of the Program's prerogative to submit the findings of the TAC to NASA HQ for official consideration. In the event of a disagreement between the Program and the TAC, NASA HQ will determine whether to fund future efforts or request additional work on this Milestone.

Due to the unavailability of data demonstrating success in reaching the milestone, no certification data package is being delivered with this report. Had the demonstration been successful within the extended time frame allotted to accommodate extenuating circumstances, namely the extended illness and unexpected death of the Principal Investigator, all or some of the following would be provided, and may be expected to be provided for future GSFC VNC demonstrations, depending on the degree of success:

A narrative report including a descriptive discussion of how the milestone was met, an explanation of each set of images, appropriate tables and summary charts, and a narrative summary of the overall milestone achievement this report serves this function.

Optical element descriptions, their significant characteristics, and their layout and purpose in the VNC descriptions of the new optical elements, the Fresnel rhomb APS are provided in full detail in a recent conference proceedings paper.[20]

A dataset consisting of contrast maps from multiple DCEs. Each DCE consists of several contrast map images. Each image would be stored in a FITS file format in $512 \times 512 \times 4$ byte floating point format or 1 MByte per contrast map. Additionally for each DCE, mean and standard deviation contrasts will be calculated and stored along with the dataset in the form of a spreadsheet. Further deliveries or distribution can be made available upon request.

Tabulation of significant operating parameters of the apparatus, including temperature stability and vibration environment. Temperature data were not recorded for this effort. Vibration data are presented in Fig. 18.

A contrast metric value as function of time over each 1000-second DCE, for target areas of 2, 3, and $4\lambda/D$ in the contrast image, in both tabular (spreadsheet) and in plotted form.

Statistical data including the contrast means and standard deviations for each DCE. Included in this report and within the spreadsheet. The Milestone was not achieved, and these data are therefore not available.

Histograms of the contrast over the set of DCEs. The Milestone was not achieved, and these are therefore not available.

8 Summary and Future Milestones

We were unable to close the WFC loop in this broadband demonstration and therefore cannot report a meaningful contrast at $2\lambda/D$, over a single DCE, let alone multiple DCEs, and many of the goals proposed for this Milestone #2 were not met. Known issues contributing to having not met these goals are presented along with mitigation paths Tab.5. The VNC requires an APS that corrects the phase difference between the two arms of the nuller to π over a sufficient bandpass for future exoplanet detection and characterization, typically on the order of $\Delta\lambda/\lambda = 0.1$. Without an APS the null is inherently narrowband due to the phase shift being set by the path length difference in the two arms of the nuller. Demonstrating the Fresnel rhomb APS remains a goal for future VNC work as a component of Milestone #3.

The plan for PI R. Lyon to run the control system as he did for TDEM Milestone #1 (PI Clampin) Milestone #2 task was never realized. Knowledge of the VNC control code was transferred by R. Lyon to B. Hicks. Ultimately, following R. Lyon's untimely death in early 2016, the team, led by B. Hicks with M. Bolcar acting as Administrative PI, ran out of time to address all known issues that are suspected of having impeded reaching the Milestone goal that hinges on closing the VNC fast wavefront control control loop developed by Lyon. Hicks and Bolcar are working to grow the VNC team and believe that given more time, there is no fundamental reason to believe the control loop cannot be closed after addressing issues presented in Tab. 5, including the rework of the aft-optics and modifications to the vacuum chamber. These two tasks are expected to be completed by September 2016.

This work was performed as a collaborative effort between R. Lyon, B. Hicks, M. Bolcar, M. Clampin, P. Petrone, T. Madison, U. Mallik, and M. Helmbrecht, and each was actively engaged with this effort. The efforts towards reaching this Milestone (Sec. 5), and the known issues and lessons learned summarized in Sec. 6.1) will serve to inform and improve performance in Milestone #3 (13-SAT13-0018), for which broadband operation remains among the success criteria.

Enabling technologies have been explored in our efforts and knowledge has been gained to continue VNC TDEM work. Future TDEM work has been advanced through both IRAD, and SBIR Phase-I and II efforts. The VNC testbed has been developed at GSFC and has run in air in a closed chamber environment, and the VNT system has been readied for vacuum operation. A simplification of the aft-optical system should improve performance and advance this next VNC/SAINT Milestone aimed at demonstrating sequential wavefront control with a macro-scale actively-controlled segmented mirror feeding the VNC to form the Segmented Aperture Interferometric Nulling Testbed (SAINT).

Ultimately meeting the Milestone #3 Success Criteria will strengthen the case that broadband and stable visible light high contrast imaging can be achieved to realize the future missions such as LUVUOIR.[4]

Bibliography

- [1] R. Morgan and N. Siegler, “Initial look at the coronagraph technology gaps for direct imaging of exoearths,” *Proc. SPIE* **9605**, p. 96052I, Sept. 2015.
- [2] M. Postman, T. Brown, K. Sembach, M. Giavalisco, W. Traub, K. Stapelfeldt, D. Calzetti, W. Oegerle, R. Michael Rich, H. Phillip Stahl, J. Tumlinson, M. Mountain, R. Soummer, and T. Hyde, “Advanced Technology Large-Aperture Space Telescope: science drivers and technology developments,” *Optical Engineering* **51**, p. 011007, Jan. 2012.
- [3] J. Dalcanton and S. Seager, “From cosmic birth to living earth: The future of uvoir space astronomy,” tech. rep., Association of Universities for Research in Astronomy, 2015.
- [4] M. R. Bolcar, K. Balasubramanian, M. Clampin, J. Croke, L. Feinberg, M. Postman, M. Quijada, B. Rauscher, D. Redding, N. Rioux, S. Shaklan, H. P. Stahl, C. Stahle, and H. Thronson, “Technology development for the Advanced Technology Large Aperture Space Telescope (ATLAST) as a candidate large UV-Optical-Infrared (LUVOIR) surveyor,” *Proc. SPIE* **9602**, p. 960209, Sept. 2015.
- [5] M. Clampin, G. Melnick, R. Lyon, S. Kenyon, D. Sassellov, V. Tolls, H. Ford, D. Golimowski, L. Petro, G. Hartig, W. Sparks, G. Illingworth, D. Lin, S. Seager, A. Weinberger, M. Harwit, M. Marley, J. Schneider, M. Shao, M. Levine, J. Ge, and R. Woodruff, “Extrasolar planetary imaging coronagraph (EPIC),” *Proc. SPIE* **6265**, July 2006.
- [6] R. G. Lyon, M. Clampin, R. A. Woodruff, G. Vasudevan, H. Ford, L. Petro, J. Herman, S. Rinehart, K. Carpenter, and J. Marzouk, “Balloon exoplanet nulling interferometer (BENI),” *Proc. SPIE* **7440**, Aug. 2009.
- [7] R. G. Lyon, M. Clampin, P. Petrone, U. Mallik, T. Madison, and M. R. Bolcar, “High contrast vacuum nuller testbed (VNT) contrast, performance, and null control,” *Proc. SPIE* **8442**, Sept. 2012.
- [8] M. Clampin, R. Lyon, P. Petrone III, U. Mallik, M. Bolcar, T. Madison, and M. Helmbrecht, “Visible nulling coronagraph technology maturation High contrast imaging and characterization of exoplanets,” tech. rep., NASA/Technology Development for Exoplanet Missions Final Report, JPL Document D-80950, https://exep.jpl.nasa.gov/technology/Clampin_Report_FINAL.pdf, 2013.
- [9] D. A. Content, N. V. Armani, C. L. Baker, C. E. Jackson, D. M. Kahle, J. W. Kruk, J. P. Lehan, M. E. Melton, E. Mentzell, J. J. Miko, D. J. Palace, B. A. Pasquale, H. L. Peabody, B. S. Smith, W. F. Smith, J. W. Stewart, D. A. Vaughn, A. Waczynski, and T. E. Wallace, “Wide field instrument preliminary design for the Wide Field InfraRed Survey Telescope,” *Proc. SPIE* **8860**, Sept. 2013.
- [10] D. Mawet, C. Hanot, C. Lenaers, P. Riaud, D. Defrère, D. Vandormael, J. Loicq, K. Fleury, J. Y. Plesseria, J. Surdej, and S. Habraken, “Fresnel rhombs as achromatic phase shifters for infrared nulling interferometry,” *Optics Express* **15**, p. 12850, Sept. 2007.
- [11] B. Hicks, R. Lyon, M. Bolcar, M. Clampin, and P. Petrone, “High-contrast visible nulling coronagraph for segmented and arbitrary telescope apertures,” *Proc. SPIE* **9143**, 2014.

- [12] B. A. Hicks, “Exoplanet detection and characterization via parallel broadband nulling coronagraphy,” *J. Ast. Tel. Inst. & Sys.* **2**, p. 011015, Jan. 2016.
- [13] M. A. Helmbrecht, M. He, and C. J. Kempf, “High-actuator-count MEMS deformable mirrors,” *Proc. SPIE* **8725**, May 2013.
- [14] W. C. Sweatt, “Reduction of Zernike wavefront errors using a micromirror array,” *Optical Engineering* **44**, p. 098001, Sept. 2005.
- [15] N. Yaitskova, K. Dohlen, and P. Dierickx, “Analytical study of diffraction effects in extremely large segmented telescopes,” *J. Opt. Soc. Am. A* **20**, pp. 1563–1575, Aug. 2003.
- [16] P. de Groot and L. Deck, “Surface Profiling by Analysis of White-light Interferograms in the Spatial Frequency Domain,” *Journal of Modern Optics* **42**, pp. 389–401, Feb. 1995.
- [17] R. J. King, “Quarter-wave retardation systems based on the Fresnel rhomb principle,” *Journal of Scientific Instruments* **43**, pp. 617–622, Sept. 1966.
- [18] P. B. Clapham, M. J. Downs, and R. J. King, “Some applications of thin films to polarization devices,” *Appl. Opt.* **8**, p. 1965, Oct. 1969.
- [19] M. R. Bolcar and R. G. Lyon, “Approaches for achieving broadband achromatic phase shifts for visible nulling coronagraphy,” *Proc. SPIE* **8445**, July 2012.
- [20] B. A. Hicks, R. G. Lyon, P. Petrone, I. Miller, M. R. Bolcar, M. Clampin, , M. Helmbrecht, and U. Mallik, “Demonstrating broadband billion-to-one contrast with the Visible Nulling Coronagraph,” *Proc. SPIE* **9605**, 2015.